HIGH PERFORMANCE FIBER LASERS WITH SPECTRAL, THERMAL AND LIFETIME CONTROL

PÄR JELGER

KTH Engineering Sciences

Doctoral Thesis
Department of Applied Physics
KTH – Royal Institute of Technology
Stockholm, Sweden 2009

High performance fiber lasers with spectral, thermal and life time control

Laser Physics
Department of Applied Physics
KTH – Royal Institute of Technology
106 91 Stockholm

ISBN 978-91-7415-504-4
TRITA-FYS 2009:65
ISSN 0280-316X
ISRN KTH/FYS/–09:65–SE

Akademisk avhandling som med tillstånd av Kungliga Tekniska Högskolan framlägges till offentlig granskning för avläggande av teknologie doktorsexamen fredagen den 11 december 2009 kl. 10.00 i sal FB52, Albanova, Roslagstullsbacken 21, KTH, Stockholm. Avhandlingen kommer att försvaras på engelska.

Cover picture: Cooperative luminescence from the 980 nm fiber laser presented in Paper VIII. (Photo by Toni Kaski)
Printed by Universitetsservice US AB, Stockholm 2009

Pär Jelger

High performance fiber lasers with spectral, thermal and lifetime control

Department of Applied Physics, KTH – Royal Institute of Technology
106 91 Stockholm, Sweden
ISBN 978-91-7415-504-4, TRITA-FYS 2009:65, ISSN 0280-316X, ISRN KTH/FYS/–09:65–SE

Abstract

This thesis contains the results of research in the fields of spectral control, efficiency and lifetime of high-power, rare-earth doped fiber lasers, properties which are of great importance for scientific and industrial applications. Volume Bragg gratings (VBGs) has for the first time been used together with fiber lasers and the laser performance in terms of spectral purity, thermal stability, and tunability was evaluated. It was found that VBGs are an excellent high-contrast spectral filter for many fiber laser designs where bulk optics are necessary, or for speciality fibers such as photonic crystal fibers or large-mode area fibers. It is also shown that they work equally well in low power and very high-power configurations, i.e. for fiber lasers ranging three orders of magnitude in output power, from ~100 mW to > 100 W. Furthermore, VBGs are shown to work very well as tunable spectral filters, producing a narrow emission linewidth in a compact setup.

Concerning efficiency, it was shown how cryogenic cooling of the fiber gain-media substantially increased the efficiency. The reasons are an increased pump absorption, an increased gain cross-section, and a decreased threshold. The broad spectral output resulting from the low temperatures is shown to be easily mitigated by implementing a VBG as one of the cavity mirrors. The low operating temperature is also shown to efficiently suppress self-pulsing in the fiber laser, which, if left unchecked, can lead to catastrophic break-down of the fiber end-faces. The increased absorption and suppressed self-pulsing allowed a fiber length long enough to almost completely absorb the pump, which meant that, for the same pump power, more than 60 % higher output-power was attained.

Finally, the lifetime issue of Yb-doped fiber lasers was addressed. It was found that Ce-codoping substantially reduced the photodarkening-rate while leaving other fiber parameters essentially unchanged. This is especially important for Yb-doped fiber lasers emitting at 980 nm, as the high inversion required make them very susceptible to photodarkening. It was shown that the output power in Yb-doped fiber lasers degraded quickly when no Ce-codoping was present and, conversely, with the right Yb/Ce-codoping ratio, degradation-free lasing could be achieved for many hours.

The research results obtained in this work could be of great interest to scientists and engineers working with spectroscopy, display systems, non-linear optics to just name a few examples.

List of Publications

This thesis is based on the following journal articles:

I. P. Jelger and F. Laurell, *“Efficient narrow-linewidth volume-Bragg grating-locked Nd:fiber laser”*, Opt. Express 15, 11336-11340, (2007)

II. P. Jelger and F. Laurell, *"Efficient skew-angle cladding-pumped tunable narrow-linewidth Yb-doped fiber laser"*, Opt. Lett. 32, 3501-3503 (2007).

III. P. Jelger, V. Pasiskevicius, and F. Laurell, *”Narrow Linewidth High Output Coupling Dual VBG-Locked Yb-Doped Fiber-Laser”*, Submitted to Opt. Express (2009).

IV. J. W. Kim, P. Jelger, J. K. Sahu, F. Laurell, and W. A. Clarkson, *"High-power and wavelength-tunable operation of an Er,Yb fiber laser using a volume Bragg grating"*, Opt. Lett. 33, 1204-1206 (2008).

V. P. Jelger, P. Wang, J. K. Sahu, F. Laurell, and W. A. Clarkson, *"High-power linearly-polarized operation of a cladding-pumped Yb fibre laser using a volume Bragg grating for wavelength selection",* Opt. Express 16, 9507-9512 (2008).

VI. P. Jelger, K. Seger, V. Pasiskevicius, and F. Laurell, *"Highly efficient temporally stable narrow linewidth cryogenically cooled Yb-fiber laser,"* Opt. Express 17, 8433-8438 (2009).

VII. M. Engholm, P. Jelger, F. Laurell, and L. Norin, *"Improved photodarkening resistivity in ytterbium-doped fiber lasers by cerium codoping,"* Opt. Lett. 34, 1285-1287 (2009).

VIII. P. Jelger, M. Engholm. L. Norin, and F. Laurell, *"Degradation free lasing at 980 nm in a Yb/Ce/Al-doped silica fiber "*,Submitted to JOSA-B (2009)

Description of Author Contribution

Paper I

I designed and performed the experiment and wrote the paper with assistance from F. Laurell.

Paper II

I designed and performed the experiment and wrote the paper with assistance from F. Laurell.

Paper III

I designed and performed the experiment and wrote the paper with assistance from V. Pasiskevicius and F. Laurell.

Paper IV

I designed the experiment and performed it together with J.W Kim. I assisted J.W Kim in writing the paper together with F. Laurell and A. Clarkson.

Paper V

I designed the experiment and performed it together with P. Wang. I wrote the paper with assistance from P. Wang, A. Clarkson and F. Laurell

Paper VI

I designed the experiment and performed it together with K. Seger. I wrote the paper with assistance from K. Seger, V. Pasiskevicius and F. Laurell

Paper VII

M. Engholm and L. Norin fabricated the fiber and measured the photodarkening. I designed the experiment comparing the efficiency between the fibers. The part in the paper relating to photodarkening was written by M. Engholm and L. Norin while I wrote the part relating to the fiber efficiency experiments with assistance from F. Laurell.

Paper VIII

I designed and performed the experiment. I wrote the paper with assistance from M. Engholm, L. Norin and F. Laurell.

Acknowledgements

I would like to express my profound gratitude to:

Professor Fredrik Laurell, my main supervisor, for constructive and excellent supervision. You gave me the opportunity to pursue a PhD in your group and it has been an invaluable experience. Your positive and inspiring attitude and encouragement have been of great importance as well as giving me the time for an uncountable number of interesting discussions. Without your support to my research activities, this thesis would not have been possible.

Professor Valdas Pasiskevicius, my co-supervisor, for sharing your extensive expert knowledge on the subject of lasers and nonlinear optics. I very much appreciate your encouragement, your constructive feed-back on difficult research issues, and for proof-reading manuscripts and conference submissions, which has been an invaluable help over the years.

Since my first trembling steps as a PhD-student three years and 344 days ago, quite a few other PhD-students have passed through the group (or are still in it). I hereby express my sincere thanks to all of you. We have had many memorable conference trips all over the world, from the US to Japan to Kista. I have tremendously enjoyed our many discussions on (im)possible laser designs and solutions, both sober and not so sober. On that subject, thanks for all the parties, both at Fredrik's and at other places. Also, thank you for being patient when the computers/servers/printers stopped working, as many times, it actually was my fault. Anyway, thanks for making the laser physics group a work environment I really enjoyed going to (almost) every morning.

I would also like to extend my gratitude to the people at Acreo AB for supplying me with, not only help and support, but also fibers over the years. Furthermore, I would like to thank Andy Clarkson at the University of Southampton for letting me into his labs during the fall of 2008.

Special thanks to my friends and family. Without your support over the years, this would not have been as an enjoyable experience as it turned out to be.

Table of Contents

1 Introduction

The Nobel Prize in physics this year (2009) was awarded to Charles K. Kao for his pioneering work on optical fibers and their use in optical communication. It was in 1965 that Kao, (together with George A. Hockham), published a paper where it was suggested to use optical fibers for low-loss guiding of light [1]. Previous experiments had shown optical fibers to be very lossy (many dB/m) but Kao et al. suggested this was not a physical limitation but merely an effect of impurities in the glass resulting in scattering and absorption losses. They also predicted that with proper fabrication techniques, losses on the order of a few dB/km should be attainable, which was 3 orders of magnitude lower than was possible at the time. A large amount of research has since then been focused on the area and today optical fibers are commercially available with losses below 1 dB/km. The transmission properties are today limited by Rayleigh scattering for shorter wavelengths and infrared absorption at longer wavelengths. It turns out that the combined losses are at their lowest around ~1.3-1.5 µm (< 0.3 dB/km), which therefore has become the preferred transmission window for optical fiber communication. The typical losses for wavelengths in the range of 0.6 µm to 1.8 µm is shown in Fig. 1.1 below.

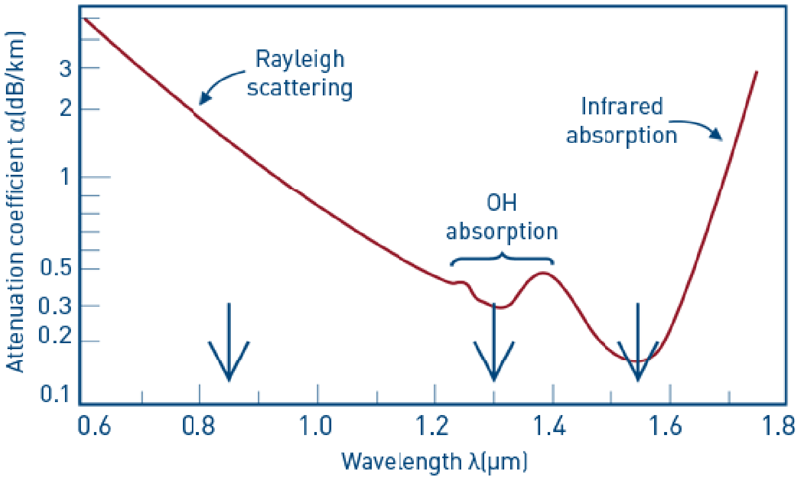

Fig. 1.1. Fiber losses for wavelengths in the range of 0.6 µm to 1.8 µm (courtesy of the Royal Swedish Academy of Science).

An optical fiber guides light through total internal reflection (TIR). This essentially means that when light propagating in an optically dense medium hits a boundary of a less dense medium at an angle below the critical angle [2], all the light is reflected. An optical fiber is therefore constructed with at least two layers: the core and the cladding. The core is the optically dense medium where the light propagates while the cladding with its less dense medium makes sure the light is confined in the core. This is illustrated in Fig. 1.2 below:

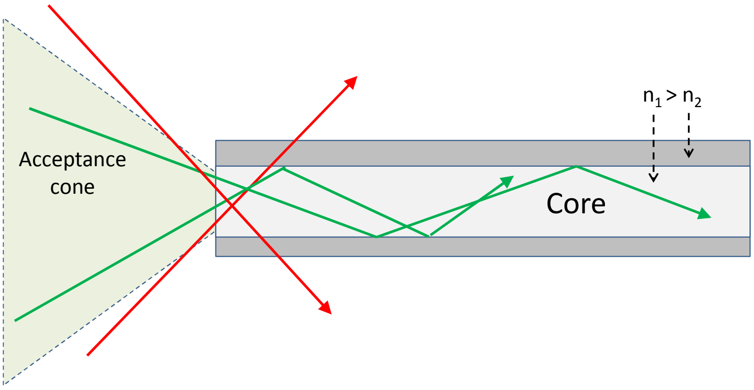

Fig. 1.2. Ray picture of light guided in an optical fiber. Here, n_1 and n_2 are the refractive index of the core and cladding, respectively.

The difference in optical denseness, or, correspondingly, the refractive index, of the core and the cladding in the fiber is what defines the transmission properties. This difference is normally expressed as the numerical aperture (NA) which is defined as

$$NA = \sqrt{n_1^2 - n_2^2} = sin(\theta_a) \tag{1.1}$$

In Eq. 1.1, θ_a is the acceptance angle of the fiber. A small NA means that only light incident on the fiber end surface at angles close to normal incidence will be guided in the fiber. Conversely, a large NA implies that light incident on the fiber even at very wide angles are guided, and that the light gathering capability of the fiber therefore is higher. The quality of the light propagating in a fiber is generally defined by the number of transverse optical modes supported by the core. The mathematical description of the allowed transverse modes is considered outside the scope of this theses but can be found in a number of textbooks, e.g. [2]. In general, single-mode operation is preferred for the propagation of a signal in the core but this is not always possible. The beam quality is quantified through its beam-parameter product (BPP) or its M^2-value. The BPP for an arbitrarily focused beam is the product of the divergence (half) angle and the spot size radius. For a diffraction limited beam, this value is equal to λ / π. The M^2-value is the wavelength independent equivalent and is simply the measured BPP divided by the minimum BPP which means that a diffraction limited beam would have an M^2-value of 1. The quality of a laser beam is also often discussed in terms of brightness where a low brightness source means a high BPP-value or M^2-value. In general, fibers often support a high brightness whereas diode lasers have a low brightness.

As can be seen in Fig. 1.1, wavelengths in the region of 1.3-1.5 μm are preferred for optical fiber communication. A considerable effort has therefore gone into developing laser sources for this wavelength region. The signal is often generated by an InGaAs or InGaAsP laser diode but, despite the low transmission loss, amplification is needed to maintain the power a long communication distance. Laser action in optical fibers was first discussed (and demonstrated) back in the 1960s [3], but it was not until the 1980s when fiber amplifiers for optical communication became of interest to the telecom industry that the field really took off [4, 5]. By doping the fibers with rare-earth elements, strong amplification can be achieved directly in the fiber without the need to manipulate the signal electronically. The main dopant used for these applications was erbium (Er), and the industry standard amplifier in telecommunication today is the erbium doped fiber amplifier or EDFA.

Although the first major application was amplification in optical fibers for the telecom industry, many other applications are today being developed. The telecom industry only took advantage of one of the many beneficial properties associated with amplification in optical fibers. Fiber lasers also have excellent heat handling capabilities thanks to the natural elongation of the gain medium. Any induced heat can therefore be dissipated over a comparatively large area without any special cooling arrangement. Secondly, the beam quality of a fiber laser is largely determined by the wave guiding properties of the fiber and is therefore unaffected by any heat induced distortion. Furthermore, the amorphous structure of glass broadens the emission spectrum of the dopant with the consequence that fiber laser often can be tuned (the wavelength shifted) over large ranges. Besides Er, many other rare-earth dopants are today used such as ytterbium (Yb), neodymium (Nd), holmium (Ho) [6], thulium (Tm) [7] and praseodymium (Pr) [8] in fiber lasers and amplifiers.

As the light is already confined in the fiber, adjusting where to direct it is relatively easy. A fiber can, for example, be mounted on a robotic arm allowing a very high degree of controllability without the need of complex optical arrangements. Furthermore, fiber lasers can be made comparatively compact since the fiber can be coiled to save space (which is not possible with a rod-type laser, for example). Today, high power fiber lasers are used in applications such as cutting, welding and marking as they can deliver a high energy beam with great precision at a relatively large distance from the target. They are also used to generate and/or amplify ultra-short pulses thanks to their broad gain bandwidths. The latter also makes them useful as tunable sources for spectroscopy applications. The precision attainable also make them useful in medical applications such as surgery.

1.1 Motivation of the Work

This thesis is focused on high power laser action in speciality fibers doped with Er, Yb, or Nd, or a combination thereof. I have investigated how to attain a narrow emission linewidth with fibers that, due to their design, are not easily spliced (coupled) to other fibers (such as FBGs), which imply that bulk components are necessary to form a laser cavity. Here, VBGs are evaluated as mirrors in fiber-laser resonators for high powers and attributes such as stability, tuning characteristics and spectral control were investigated for different fiber types and different output powers. In the last decade, volume Bragg gratings (VBG), has attracted a great deal of interest. Originally, this component was used to lock diode lasers [9] and as a resonator in compact solid-state lasers at moderate powers [10].

It is found in this thesis that VBGs work exceedingly well as cavity delimiters for fiber lasers with output powers ranging from ~100 mW to ~100 W with maintained spectral characteristics. Furthermore, the thesis covers other experiments where the use of a spectral filter such as a VBG greatly enhances the usefulness of the laser source. These include cryogenically cooled, highly efficient fiber lasers and long lifetime photodarkening resistant fiber lasers operating at 980 nm.

From an application point of view, these results have strong implications on the laser technology development as it enables compact, simple and highly efficient narrow linewidth fiber lasers. Cryogenic cooling shows how the efficiency and stability can be increased for Yb-doped fiber lasers. Furthermore, the photodarkening resistant fibers evaluated are shown to have a large impact on the expected lifetime of Yb-doped fiber lasers, especially when operating at 980 nm. This is, of course, important for industrial applications where a large number of service-free operation hours are expected.

1.2 Outline of the Thesis

The thesis summarizes the research presented in papers I-VIII and gives a relevant theoretical background to the subject. It is outlined as follows: In Chapter 2, theory related to optical fibers is presented. This includes the spectral properties of the rare-earth doped glass materials making up the fibers. The necessary equations describing laser oscillation in optical fibers are presented together with simulations. Furthermore, the spectral properties of fiber lasers are discussed together with solutions for how to lock and stabilize the emission spectrum. Finally, problems such as self-pulsing and photodarkening are discussed.

In Chapter 3, the theory of VBGs is described. Calculations showing the important fabrication and material properties are presented and we discuss how they affect the spectral properties of the VBG. Furthermore, the limitations of VBGs in terms of tuning range, beam quality requirements and heat effects are also discussed.

In Chapter 4, the experimental conditions and results from Papers I-VIII are described in more detail. An effort is made to put the research into its broader context and to clarify how the different results are related to each other. It starts out with the initial proof-of-concept experiments carried out with a VBG-locked Nd-doped fiber laser (Paper I). The fiber had a microstructured large-mode area core and was consequently not easy to splice. The experiment showed promising results with regards to emission spectrum and efficiency when compared to a free-running cavity delimited by a mirror. A follow-up experiment was carried out with an order of magnitude higher output power using an Yb-doped fiber (Paper II). This fiber was mounted in a way which permitted tunable operation of the laser and the results showed a very good efficiency with narrow linewidth emission over a large tuning range. In Paper III, this was extended to include two VBGs which were detuned with respect to each other. It allowed the laser cavity to lock on to the reflection peak of one of the VBGs and on a side-lobe of the other. This construction opens up for an adjustable output coupling with increased spectral selectivity.

In Paper IV-V, the output power of the fiber laser was again increased 1-2 orders of magnitude. Tunable operation was examined in a compact Er/Yb fiber laser setup with a beam quality which was far from diffraction limited. Furthermore, a high-power linearly polarized narrow linewidth fiber laser was constructed and the implications of thermal load in the VBG were studied. The results showed a stable and efficient output power despite the fact that the VBG was heated through a small absorption of radiation. The latter could be seen through a slightly shifted oscillation wavelength.

In Paper VI, it is shown how cryogenic cooling can be used to reduce the lasers susceptibility to self-pulsing as well as increases the efficiency. The drawback of this technique is a broadening of the emission spectrum which, however, can be mitigated by the introduction a VBG with a carefully selected reflection wavelength in the cavity.

Photodarkening is a serious degradation phenomena for fiber lasers where the absorption is successively increasing in the fiber with time. The output power is then reduced correspondingly. To reduce this problem, Ce-codoping of the core was investigated in Paper VII. A Yb-doped fiber co-doped with Ce was evaluated for any signs of efficiency reduction related to its photodarkening resistivity, and very promising results were obtained. The same fiber was then used to construct a laser which was locked with a VBG at a transition highly susceptible to photodarkening, and the results were compared to two non-photodarkening resistant fibers. These experiments show degradation-free operation of the

Ce-codoped fiber for several hours while the conventional fibers degraded at a very high rate.

In Chapter 5, the conclusions for this thesis are summarized. Finally, appended at the end of the thesis are the journal articles this thesis is based on.

2 Fiber Laser Theory

2.1 Fiber Basics

The industry standard optical fiber for telecommunication has a core diameter of 8 µm and a cladding diameter of 125 µm. Apart from providing a flexible and durable fiber material, it ensures single-mode operation in the telecom wavelength region (~1.3-1.5 µm) with remarkably low losses (< 1 dB/km). While it would be attractive to use this standard for other applications as well, the small core does present a problem. Initial experiments were typically based on flash-lamp pumping but for today's high power fiber lasers, a more efficient pumping technique is necessary, and high efficiency laser diodes are now preferred as a pump source. As laser diodes in general are of low brightness, it is difficult to reach high launch efficiency into a core area of telecom size. Furthermore, for high powers, a small core area is also much more susceptible to various nonlinear effects since these effects are strongly intensity dependent.

Today, a common solution to this is to design active fibers with two claddings, so called double-clad (DC) fibers (see Fig. 2.1(a)). The pump radiation can then be launched into the first cladding surrounding the core (see Fig. 2.1 b). As the pump radiation propagates in this inner cladding, part of it will overlap with the core where it can be absorbed. Obviously, this will result in a lower pump absorption per unit length, but this can, to a large extent, be compensated for by increasing the dopant concentration in the core. The benefit here is that this inner cladding can be designed for maximum light gathering with a high numerical aperture (NA) and a large area without affecting the mode quality of the laser radiation which propagates in the core. One potential problem with cladding pumping is a reduction in the absorption due to persistent symmetrical cladding modes which never overlap the core. This can be resolved by careful design of the cladding [11-13], e.g. a polygonal cladding shape [14]. For medium power applications (~100 W), the outer cladding confining the pump radiation is often the fiber coating which then consists of a low-index acrylic compound.

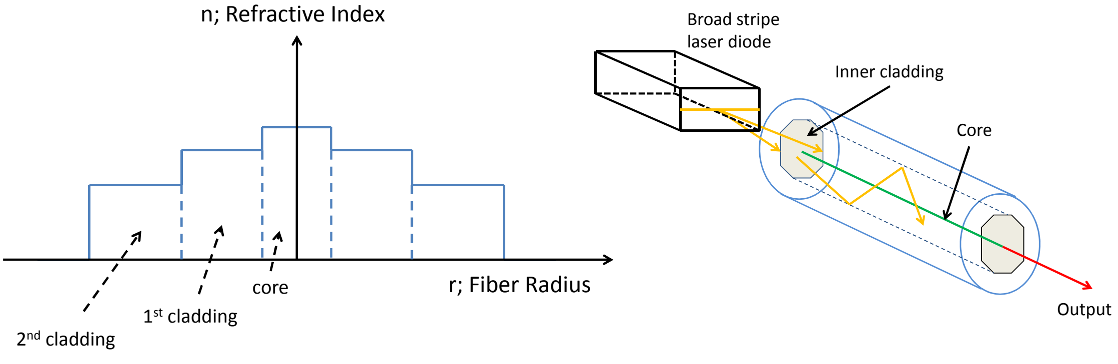

a) b)

Fig. 2.1. a) Refractive index for double-clad fiber. b) Laser diode pumping of double-clad fiber.

To increase the resilience against nonlinear parasitic effects, large-mode-area (LMA) fiber designs are today quite common. In standard silica fibers, core sizes with up to ~30 µm diameter and close to single-mode performance are commercially available. The limiting factor here is the NA (defined in Chapter 1) which has to be rather low (< 0.06) in order to only support a few modes, corresponding to a decent mode quality. A useful parameter here is the normalized frequency number or V-number defined as:

$$V_{nr} = 2\pi \frac{a}{\lambda} NA \tag{2.1}$$

Here a is the core radius and λ is the wavelength in the core. It turns out that for step index fibers, a V-number below 2.405 ensures single-mode operation. This is actually the first root of the Bessel function, J_0, which in turn is a solution to the wave equation for propagation in a cylindrical waveguide (for more information, see any standard text book such as [2]). For larger V-numbers, the transverse mode volume is approximately equal to $V_{nr}^2 / 2$.

With a too low NA, the guiding properties of the fiber will weaken and the micro-bending losses will increase. An alternative to reducing the NA to get single-mode operation is to coil the fiber, which reduces the symmetry of the waveguide and, thus, introduces losses for higher-order modes [15]. This can also have a positive effect on the pump absorption but one has to be careful not to change the coiling structure when working with active fibers sensitive to photodarkening. It has been shown that the squeezed mode in a coiled fiber might not be able to extract all the power from the core, resulting in spatially dependent optical losses [16]. Photodarkening is discussed later in the chapter.

In recent years, photonic crystal fibers (PCF) have become popular as gain fibers. The term PCF-fiber is used for many types of fibers with the common ground that all of them have a transverse micro-structuring which, in one way or another, influences the transmission properties of the fiber [17]. This has, for example, been used to enable even higher core areas while maintaining single-mode operation [18]. With the addition of an air-confined inner cladding, very high NAs have also been achieved [19]. Moreover, bandgap-guiding has enabled lasing in gain regions which are otherwise inaccessible [20]. A potential drawback of these fibers is the sensitivity to contamination of the micro-structure e.g. through dust particles entering the holes. Furthermore, low-loss splicing can be difficult.

For many applications, emission with a single polarization state is of great importance, e.g. nonlinear frequency conversion. To enable a high polarization extinction ratio in optical fibers, glass rods with a smaller thermal expansion coefficient than that of the fiber can be inserted on opposite sides of the core. After the fiber drawing, they will then exert a continuous pressure on the core, making it birefringent. While the same technique can be used in PCF-fibers, careful tailoring of the bandgap structure has also produced polarizing fibers, eliminating the need of other polarizing elements in the cavity [21].

2.2 Pumping Techniques

The first fiber lasers were transversely pumped by winding the fiber around a flash lamp [22], however, this technique is rather unusual today. Other techniques such as V-groove side-pumping [23], diffraction-based side-pumping [24] and fiber disc lasers [25] have also been investigated but the most simple and common method is probably so-called end-pumping. With high NA claddings, low brightness sources such as laser diodes can, with a high efficiency, still be launched into the fiber. The fiber cladding's ability to collect light depends mainly on the cladding radius and the NA. This can be understood from the beam propagation factor (defined as $\omega_r \times \theta_{1/2}$ see Chapter 1), which describes the brightness of the incident light and depends on the minimum spot size and the divergence half-angle. A low brightness source (high beam propagation factor) therefore requires a fiber with a large cladding radius and/or a large NA if coupling efficiency is to be achieved.

While end-pumping is convenient, it can present a challenge to separate the pump from the signal radiation. Furthermore, the signal radiation usually has a much higher beam quality and can thus easily destroy the pump source if allowed to be coupled back with the pump. The usual way to separate the pump and the signal in end-pumped configurations is by a dicroic mirror. However, when the signal and pump are close in wavelength, i.e. at a low quantum defect, it is difficult to fabricate dicroic mirrors with a high spectral discrimination.

An alternative way to separate the pump and the signal is by skew-angle pumping (Paper III). By not filling the NA of the cladding, the signal and pump can now be separated spatially. A schematic of this is shown below in Fig. 2.2. The pump convergence angle must be smaller than the acceptance angle of the cladding minus the acceptance angle of the core, where the acceptance angle is defined as $\theta_{accept} = arcsin(NA)$.

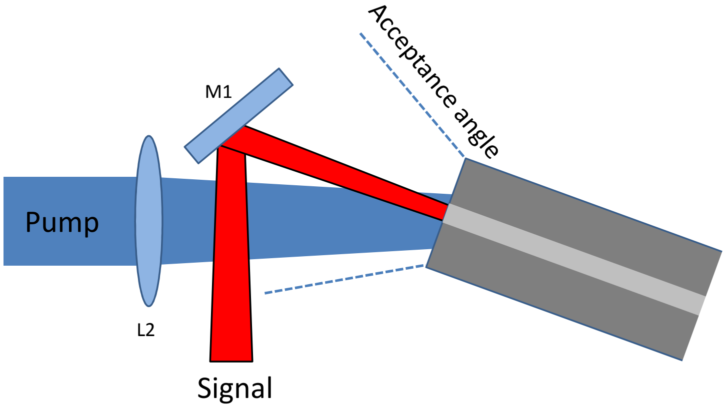

Fig. 2.2. Schematic of skew-angle pumping. The blue beam is pump and the red beam is signal. M1 is any highly reflective folding mirror and L2 is a large NA lens used to focus the pump light.

2.3 Yb, Er/Yb and Nd-doped Silica Glass

In this thesis, all of the laser materials used were composed of rare-earth ions from the lanthanide group doped into the silica glass. The electron configuration of trivalent lanthanide ions provides a strong shielding of the 4f-state with the resulting effect that the ions will, to a large extent, act as free ions. A more comprehensive discussion on this subject can be found in standard text-books such as [26, 27]. The silica glass host, in contrast to a solid-state crystal host, can be very flexible in incorporating ions into its matrix which is an effect of the amorphous structure of the glass, although for pure silica, clustering and crystallization can be a problem even at small concentrations [28]. However, by codoping with aluminum, this can to a large extent be mitigated [29]. The amorphous structure of rare-earth doped glasses will also strongly affect the line broadening mechanisms which differ substantially from that of the crystalline host materials.

Silica glass hosts are subject to both homogeneous and inhomogeneous broadening [30]. At room temperature, rare-earth doped silica glass is mainly homogeneously broadened which is a result of phonon broadening of the different Stark components. These are strongly coupled within each Stark-split manifold through the rapid emission and absorption of phonons which take place on a sub-ps timescale [31]. This effect is also responsible for the thermal population of the higher Stark components. In crystal hosts, these Stark-split energy levels can usually be resolved as discrete lines. In glass hosts however, these lines can in most cases not be resolved except at temperatures close to absolute zero.

The inhomogeneous part of the broadening comes from the amorphous nature of the glass structure. Each individual ion in the glass matrix will experience different crystal field parameters [26]. This also implies that the inhomogeneous broadening is more or less temperature independent.

The gain for a certain wavelength is determined through the absorption and emission cross-sections. Ideally, these should be measured directly, but unfortunately this is quite difficult with optical fibers [32]. One possible approach is to use the Einstein A and B coefficients to calculate the cross-sections through the Ladenburg-Fuchtbauer relation [33]. However, the validity of this relation depends on that either a) all of the Stark-components must be equally populated in the two manifolds or b) all of the transitions must have the same strength which is the implicit requirement for the Einstein relation to apply. In reality, this is seldom the case resulting in erroneous values for the cross-sections.

If only one of the cross-sections could be determined, the McCumber theory [34] can be used to determine the other [35, 36]. The relationship between the cross-sections is given by Eq. 2.1 below:

$$\sigma_{a,b} = \sigma_{b,a} e^{\left(\frac{\varepsilon - h\nu}{k_B T}\right)} \tag{2.1}$$

Here, $\sigma_{a,b}$ and $\sigma_{b,a}$ are the two related cross-sections, ε is related to the partition function, $h\nu$ is the photon energy and $k_B T$ is the thermal energy. The McCumber relation assumes that the time it takes to establish a thermal distribution within each manifold is short compared to the manifold lifetime and that the linewidth of each Stark-level is narrow compared to the thermal energy, $k_B T$. While the first of these requirements is generally fulfilled, the second is not always true for amorphous hosts. Although initial research showed that this could cause problems when calculating cross-sections in glass hosts [37], it has later been shown that the relation is sufficiently accurate for many dopants at room temperature [38].

One of the more common rare-earth ions is neodymium (Nd). Although many lasing configurations are possible, the most common one is pumped at 808 nm with laser emission at 1064 nm which corresponds to a transition from the ${}^4F_{3/2}$ manifold to the ${}^4I_{11/2}$ manifold. At room temperature, the ${}^4I_{11/2}$ level lies $\sim 10k_BT$ above the ground state which, together with the fast nonradiative relaxation from this level, prevents population buildup. This means that Nd-doped lasers operate as 4-level lasers in this configuration. For Nd^{3+} in a silica host, a typical value for the emission cross-section is $\sim 1.4\times 10^{-20}\,cm^2$ and the radiative lifetime $\sim 500\mu s$. The energy levels and fluorescence spectra are found below in Fig. 2.3 (a) and (b), respectively.

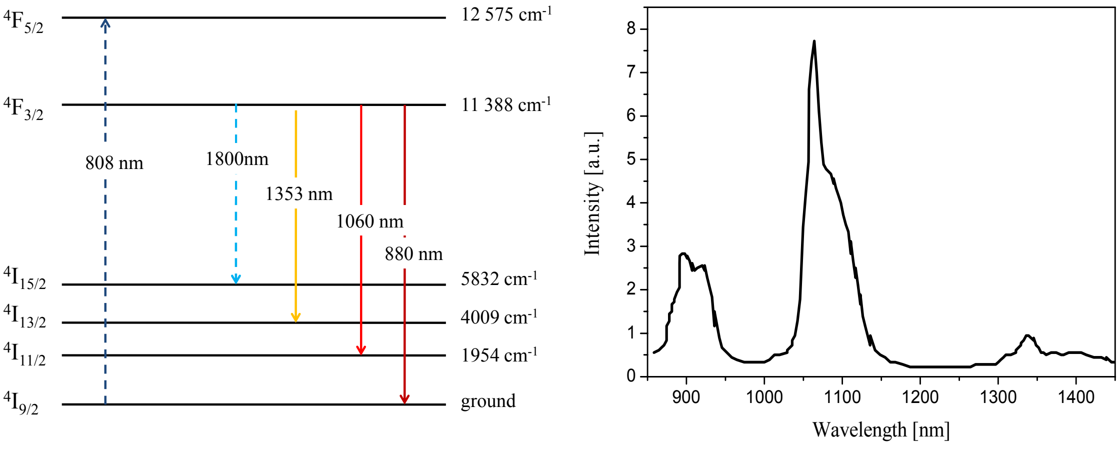

a) b)

Fig. 2.3. a) Energy levels of Nd-doped silica glass. b) Shape of fluorescence spectra from Nd-doped silica glass pumped at 808 nm [39]

For telecom applications, erbium (Er) is a very common dopant for silica fiber lasers and amplifiers due to its broad gain bandwidth around 1.5 µm. The reason is of course that it overlaps with the low loss transmission window in silica fibers as was explained in Chapter 1. This emission corresponds to the transition ${}^4I_{13/2} \rightarrow {}^4I_{15/2}$ which is 3-level in nature. Er is often codoped with ytterbium (Yb) to facilitate pumping as the absorption cross-section of Yb is considerably larger than that of Er. The Er/Yb pumping arrangement is illustrated in the energy level diagram in Fig. 2.4 (a). The Yb-ion absorbs a photon at 980 nm which then is transferred from the ${}^2F_{5/2}$ level in Yb to the ${}^4I_{11/2}$ level in Er. The two energy levels are very close in energy but the latter has a considerably shorter lifetime and decays almost instantly to the upper laser level $^{4}I_{13/2}$. The absorption and emission spectrum of Er for the 1.5 µm transition is shown in Fig. 2.4 (b).

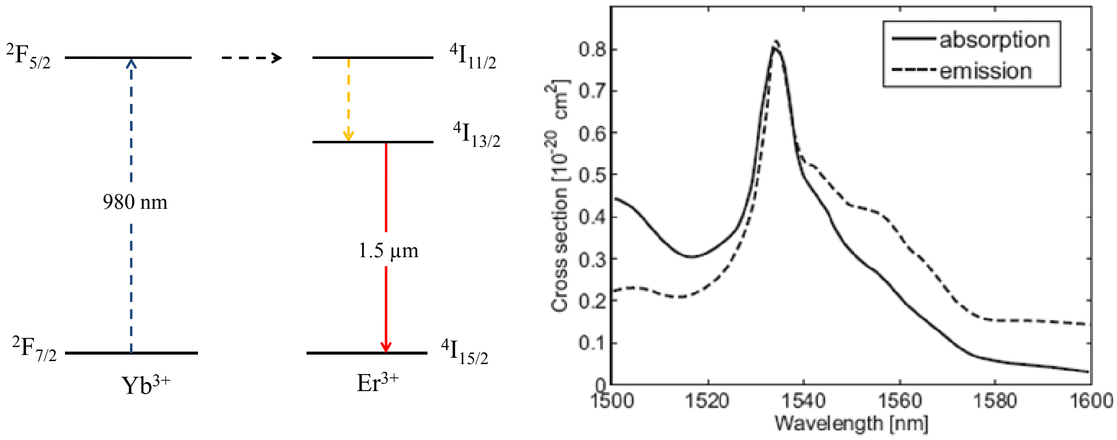

a) b)

Fig. 2.4. a) Energy level diagram of Er/Yb codoped silica. b) Absorption and emission spectrum of Er-doped silica.

In the last decade, Yb-doping has become increasingly popular for high-power fiber lasers application, much due to the very high slope efficiency reachable with this ion. The reason for this can be understood if we look at the energy level diagram of the Yb-ion in silica seen in Fig. 2.5 (a). All laser action takes place between the two stark-split manifolds $^{2}F_{5/2}$ and $^{2}F_{7/2}$. This simple structure removes the problem with excited state absorption (ESA) common in other rare-earth ions. Furthermore, the narrow spacing of the Stark-lines provides an almost continuous absorption band which stretches from 850 nm to 1070 nm. The reciprocal is also true, which means that fluorescence emission can be seen from 940 nm to almost 1200 nm. This, in combination with high emission and absorption cross-sections, makes Yb a very useful dopant (see Fig. 2.5 (b)).

At high doping levels, quenching can become a problem. This manifests itself as a loss of pump photons as electrons in the $^{2}F_{5/2}$ state relaxes nonradiatively by transferring part of their energy to the neighboring ions. The exact process is not fully understood but even a small number of quenched ions can lead to a loss of inversion [40]. A high Yb concentration, in combination with a high inversion, is also susceptible to the formation of color-centers, i.e., photodarkening, a subject which will be treated later in this chapter. The lifetime of the upper laser level in Yb-doped silica is ~ 850 µs.

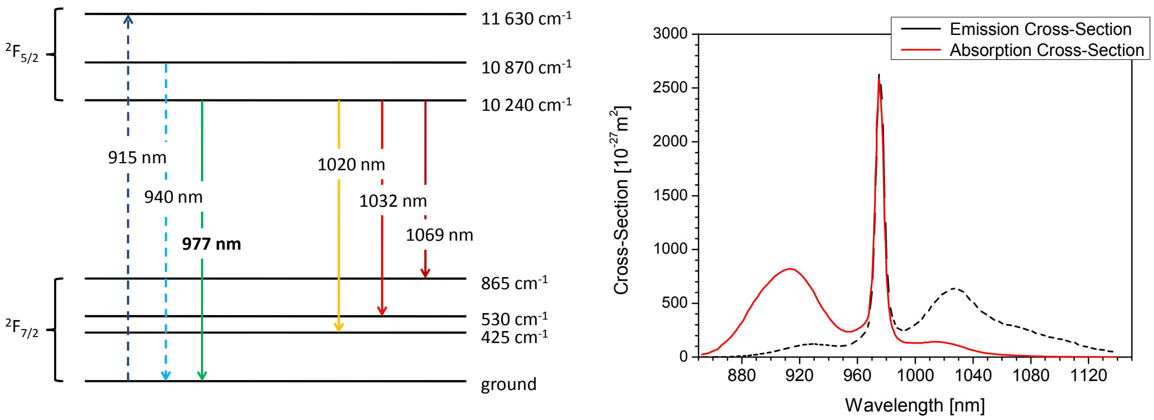

a) b)

Fig. 2.5. a) Energy level diagram of Yb-doped silica. b) Emission and absorption cross-sections of Yb-doped silica [41].

2.4 Spectral Control

The broad gain curve of rare-earth doped fiber lasers makes it difficult to achieve a narrow emission linewidth. It is not uncommon to see linewidths of more than 10 nm full-width-half-maximum (FWHM). For applications such as marking, drilling or welding, this is of little importance. For spectroscopy or non-linear conversion processes, however this necessitates the use of a spectral filter in the cavity, such as an etalon, or that one (or both) of the resonator mirrors has a high spectral contrast. For low power applications, fiber Bragg gratings (FBGs) are a convenient way to wavelength-stabilize a fiber laser. As the name implies, FBGs are constructed by introducing a periodic modulation of the refractive index into the core of the fiber. This periodic modulation then forms a Bragg-structure [42] which will reflect any wavelength fulfilling the Bragg-condition (more on this in Chapter 3). Although the use of FBGs have been reported in a few higher power experiments [43], they have certain drawbacks: They generally require single-mode fibers to work properly as different propagating transversal modes otherwise would experience different peak reflectivity wavelengths. Furthermore, FBGs are not easily tunable; the only means available are by stretching, compressing or by varying the temperature of the FBG [44]. In any case, the tuning range is quite limited and can in the first two instances lead to fiber fracturing. Moreover, fiber types such as PCF and certain LMA fibers are difficult to splice to FBGs while maintaining low losses [45].

For free-space applications, diffraction gratings such as replica diffraction gratings have previously been a common way to frequency stabilize fiber lasers as well as other types of solid-state lasers [46]. By placing the grating in the Littrow configuration, tunable operation is also possible [47]. However, the bandwidth of the grating depends on the illuminated grating area, resulting in the need of large telescope arrangements in order to achieve narrow emission linewidths. Furthermore, unless the zero:th order of the grating is used as the output of the laser, this power will be lost which lowers the efficiency of the system. On the other hand, if the zero:th order is used to couple out the laser radiation, the output beam direction will change every time the laser is tuned to another wavelength. See Fig. 2.6 for an illustration of a surface diffraction grating.

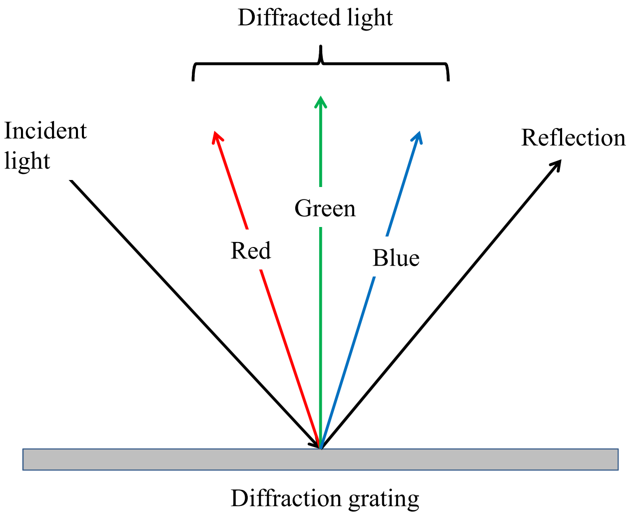

Fig. 2.6. Schematic illustration of the spectral response of a diffraction grating.

In recent years, volume Bragg gratings (VBGs) have attracted a great deal of attention as frequency stabilizing free-space components. VBGs are bulk glass components with a periodically modulated refractive index profile such as in the FBGs but with apertures of up to ~cm^2. As VBGs have been used extensively in this work, they are handled separately in Chapter 3.

2.5 Theoretical Modeling of Yb-doped Fiber Lasers

In general terms, the amplified power for a signal of initial power $P(0)$ and with a wavelength λ for a given transition, after a fiber of length L, can be written as [48]:

$$P(L) = P(0)\cdot e^{\int_0^L \left(g^*(\lambda)\cdot n_2(z) - \alpha(\lambda)\cdot n_1(z)\right)dz} \tag{2.2}$$

In Eq. (2.2) above, n_2 and n_1 are the fractional populations in the upper and lower laser level, respectively, and $g^*(\lambda)$ and $\alpha(\lambda)$ are the Giles parameters defined as:

$$\begin{aligned} g^*(\lambda) &= \Gamma(\lambda)\sigma_{21}(\lambda)n_t \\ \alpha(\lambda) &= \Gamma(\lambda)\sigma_{12}(\lambda)n_t \end{aligned} \tag{2.3}$$

Here, $\Gamma(\lambda)$ is the overlap factor between the normalized optical mode and the dopant distribution in the fiber. σ_{21} and σ_{12} are the emission and absorption cross-section, respectively, and n_t is the density of the active Yb-ions. Although the population in the two laser levels will vary depending on parameters such as fiber position, pumping, and laser configuration, it is instructive to look at what the gain will be for a given fractional population difference in n_2 and n_1 obeying the relationship $n_1 + n_2 = 1$. This is generally done by examining the gain cross-section which can be found by dividing the two terms inside the integral in Eq. 2.2 with the Yb-ion density n_t:

$$g = \left(g^* n_2 - \alpha n_1\right)\Big/ n_t = \sigma_{21}n_2 - \sigma_{12}n_1 \tag{2.4}$$

For simplicity, we have set $\Gamma(\lambda) = 1$ which implies that the optical mode overlaps perfectly with the doped region. In a 4-level system, the lower laser level will deplete fast enough to be considered empty which means that the gain cross-section will simply be given by the emission cross-section times the normalized upper laser level population. In the quasi-3-level case, which corresponds to the emission above 1 μm in Yb-doped fiber lasers, the lower laser level is still partially populated. The gain cross-section is plotted in Fig. 2.7 for population inversions from 10% to 100% (full inversion). It is evident that the gain at 980 nm quickly overtakes the gain above 1 μm for inversion levels above 50 %. It is, of course, not possible to get an inversion above 50 % unless you pump at 920 nm or 940 nm.

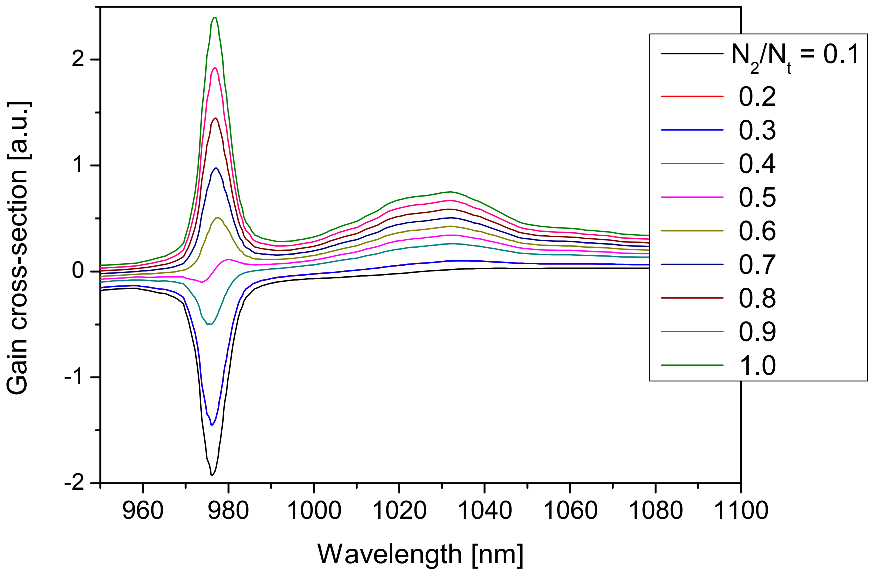

Fig. 2.7. Gain cross-section for various inversions.

The general approach to determining the actual population inversions as well as the gain and output power of a laser system is by combining the laser rate equations, which describe the possible energy transitions in the laser, with equations governing the evolution of the pump and the signal along the fiber. Regardless if the actual system operates in the 3-level, quase-3-level or in the 4-level regimes, it is usually sufficient to use a 2-level model to simulate its behavior. This is illustrated in Fig. 2.8 (a) and (b) below for a 4-level system and a quasi-3-level system.

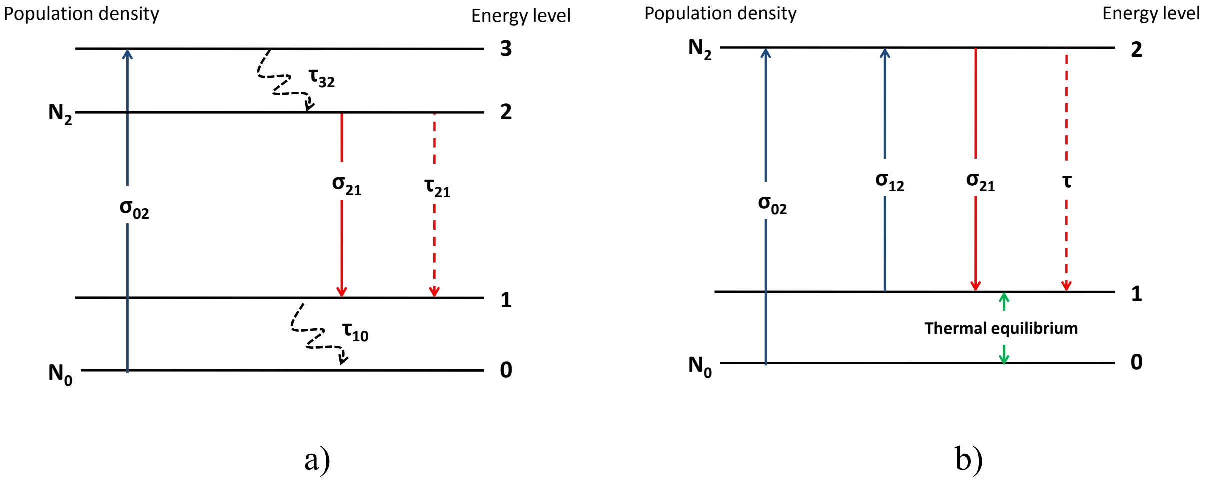

Fig. 2.8. a) Energy level diagram for a 4-level laser. b) Energy level diagram for a quasi-3-level laser.

In Fig. 2.8 (a) above, the lifetimes τ_{32} and τ_{10} are assumed to be short (almost zero) and the only populations of interest are therefore N_0 and N_2. In Fig. 2.8 (b), we pump directly into the upper laser level. Here, however, the lower laser level is part of the same manifold as the ground state and the populations within those levels are therefore described by the Boltzmann-distribution function. Again, this means that the only two populations of interest are N_0 and N_2. For a quasi-3-level laser such as an Yb-doped fiber laser, the pump and signal rate equations are written as:

$$\begin{aligned}
\frac{dI_P}{dz} &= -\Gamma_P I_P \cdot \left(\sigma_{abs}^{P} N_0(z) - \sigma_{em}^{P} N_2(z)\right) \\
\frac{dI_{S_i}^{\pm}}{dz} &= \pm\Gamma_S I_{S_i}^{\pm} \left(\sigma_{em}^{S_i} N_2(z) - \sigma_{abs}^{S_i} N_0(z) - \alpha_{loss}\right) \pm 2\sigma_{em}^{S_i} \frac{N_2(z)}{A_{core}} \frac{hc^2}{\lambda_i^3} \Delta\lambda_i
\end{aligned} \tag{2.5}$$

In the rate equations above, I_P is the pump intensity, $I_{S_i}^{\pm}$ is the forward (+) and backward (-) propagating signal intensities for the i:th wavelength (λ_i) and $\Gamma_{S,P}$ is the overlap factor for the signal or the pump radiation with the doped core, respectively. N_0 and N_2 are the ground state population density and upper laser level population density, respectively. Furthermore, σ_{abs} and σ_{em} are the absorption and emission cross-sections, respectively, for the signals or the pump as indicated by the superscript and A_{core} is the core area. The last term in the rate-equation for the signals is the amplified spontaneous emission (ASE). For lasers emitting around 1030 nm, this term can often be omitted as the oscillating signal will be many orders larger. The corresponding rate equation for the ground state population is:

$$\frac{dN_0}{dt} = \sum_i \frac{\left(I_{S_i}^{+} + I_{S_i}^{-}\right)}{h\nu_{S_i}} \left(\sigma_{em}^{S_i} N_2 - \sigma_{abs}^{S_i} N_0\right) + \frac{I_P}{h\nu_P}\left(\sigma_{em}^{P} N_2 - \sigma_{abs}^{P} N_0\right) + \tau^{-1} N_2 \tag{2.6}$$

The reabsorption caused by the thermal population of the lower laser level will increase the threshold but the power is not lost. When simulating continuous lasers, it is generally sufficient to examine the steady-state solution which means that we can set the left hand side of Eq. 2.6 to zero ($dN_0/dt = 0$). Let us now assume that the signals overlap well with the dopant, ($\Gamma_S \approx 1$), the steady-state population can then be written as:

$$N_0 = N_t \cdot \frac{\sum\limits_{\lambda} \frac{\left(I_{S_i}^{+} + I_{S_i}^{-}\right)}{h\nu_{S_i}} \sigma_{em}^{S_i} + \frac{I_P}{h\nu_P} \sigma_{em}^{P} + \tau^{-1}}{\sum\limits_{i} \frac{\left(I_{S_i}^{+} + I_{S_i}^{-}\right)}{h\nu_{S_i}} \left(\sigma_{em}^{S_i} + \sigma_{abs}^{S_i}\right) + \frac{I_P}{h\nu_P}\left(\sigma_{abs}^{P} + \sigma_{em}^{P}\right) + \tau^{-1}} \tag{2.7}$$

$$N_t = N_0 + N_2$$

For oscillation to build up, a cavity is needed. Although many types of cavities are possible, the one by far simplest is a linear cavity delimited by two mirrors. For efficient lasing, one of the mirrors is usually highly reflective while the other is used to couple-out part of the oscillating radiation.. A schematic of a linear cavity is shown in Fig. 2.9 below where reflectivities are given by R_1 and R_2.

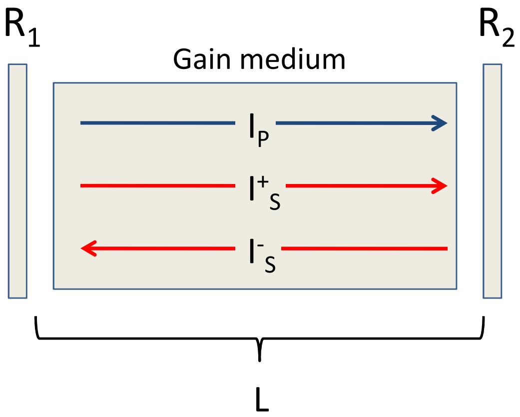

Fig. 2.9. Schematic illustration of a linear laser cavity.

The boundary conditions at the mirrors for each signal (+/-) are then given by:

$$\begin{aligned} I_{S_i}^{+}(0) &= (1 - R_1(\lambda)) \cdot I_{S_i}^{-}(0) \\ I_{S_i}^{-}(L) &= (1 - R_2(\lambda)) \cdot I_{S_i}^{+}(L) \end{aligned} \tag{2.8}$$

If there were no losses in the cavity (except for the outcoupling), the rate equations in Eq. 2.5 can actually be solved analytically with a Rigrod analysis [49]. Without going into the details, the solution is based on the assumption that the product of the forward- and backward-traveling signal intensities is constant at any point in the fiber ($I_S^{+}(z) I_S^{-}(z) = const$). The output at the second mirror can then be written as:

$$I_2 = \frac{(1-R_2)I_{sat}}{\left(1+\sqrt{R_2/R_1}\right)\left(1-\sqrt{R_1R_2}\right)} \cdot \ln\left(G_0\sqrt{R_1R_2}\right) \qquad (2.9)$$

In Eq. 2.9, I_{sat} is the saturation intensity and G_0 is the small signal gain. From Eq. 2.9, we can also derive the output power ratio from the two reflectors which becomes:

$$\frac{P_1}{P_2} = \frac{1-R_1}{1-R_2}\sqrt{\frac{R_2}{R_1}} \qquad (2.9a)$$

If we ignore the saturation intensity which only acts as a scale factor here and set $G_0 = 30$ dB in Eq. 2.9a, we get the following results for the output-power, P_2, for three different values of R_1 (100 %, 99 % and 90 %).

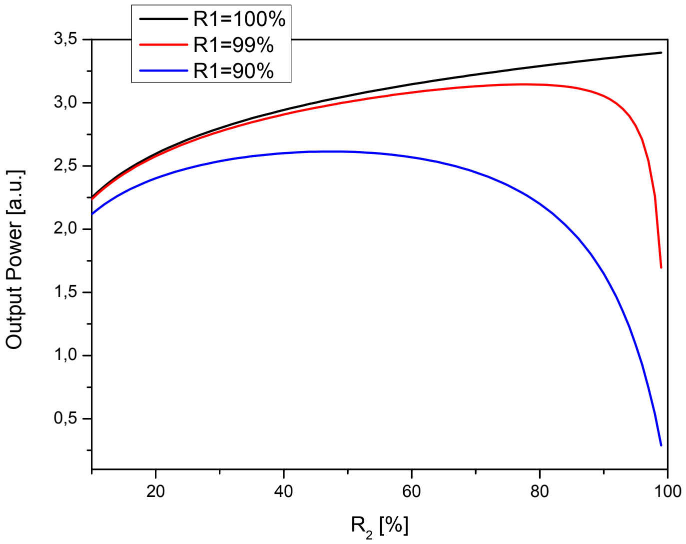

Fig. 2.10. Calculated output intensity using Rigrod analysis.

From Fig. 2.10, it might seem that a high reflectivity is needed in order to achieve a high efficiency. In reality, parasitic cavity losses will have a large effect on the optimal reflectivity of the outcoupling mirror. It turns out that the slope efficiency depends on the ratio of the outcoupling losses to the total round-trip losses including the parasitic cavity losses [26]. This can be shown by numerically solving the two-point boundary problem defined by the cavity and the rate-equations in Eq. 2.5. For simplicity, only one signal is now assumed to oscillate in the cavity (no ASE). The simulation is based on the assumption of a 0.04 dB/m transmission loss in the fiber and 4 % Fresnel losses from the end faces of the fiber. The fiber is set to have a 20 µm core and a 400 µm cladding diameter with a pump absorption of ~1.2 dB/m. In Fig. 2.11, the output power as a function of outcoupling reflectivity is plotted for two pump powers: 5 W and 25 W, respectively. In Fig. 2.11 (b), the slope efficiency (power extraction efficiency above threshold) is plotted against the outcoupling reflectivity.

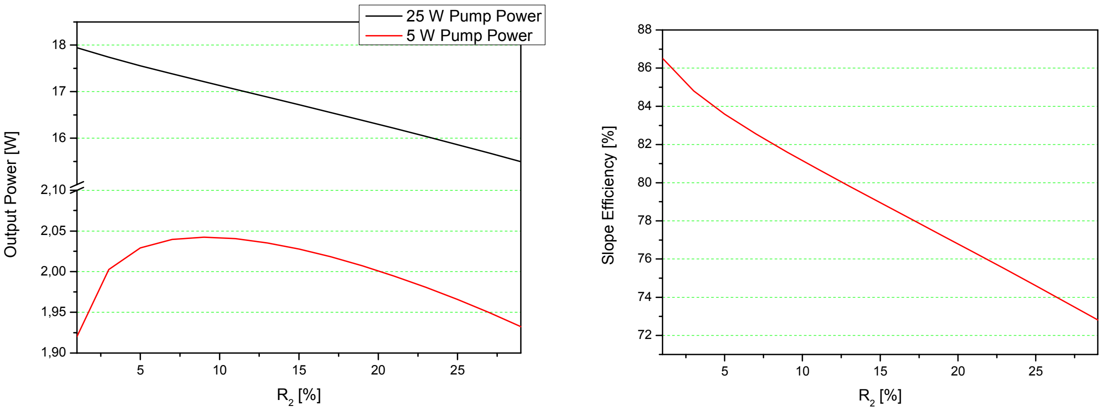

a) b)

Fig. 2.11. a) Simulated output powers for 5 W and 25 W pump powers. b) Simulated slope efficiency.

It can be seen in Fig. Fig. 2.11 (a) that only for pump powers close to threshold does the outcoupling have a practical optimal value. For higher pump powers, a higher outcoupling is preferred. This can also be seen in Fig. 2.11 (b) where the slope efficiency clearly decreases with increasing reflectivity (decreasing outcoupling).

For three-level lasers like the 980 nm transition in Yb, other problems arise. To reach transparency of the laser medium when pumping at 915 nm, a population inversion of ~50 % is needed. However, at this pump level, the gain above 1 μm will far surpass the gain at 980 nm. This can be seen if we examine the gain relations for the three different gains of interest when pumping at 915 nm [40, 48]. Let us start with defining the logarithmic gain G_λ for a given wavelength λ as:

$$G_\lambda = log_{10}\left(e^{g^*(\lambda)\cdot n_2 - \alpha(\lambda)\cdot n_1}\right) \tag{2.10}$$

Here, λ is 915 nm, 980 nm and 1030 nm, respectively. The gain relations for these three regions of interest can then be written as in Eq. 2.11, where we have assumed that there is no positive gain at 915 nm and no reabsorption above 1 μm. This is not strictly true, but it will simplify the calculations below and only influence the results to a minor degree. As could be seen earlier, in Fig. 2.7, the effective gain above 1 μm will have its highest value around 1030 nm and we will henceforth let the gain above 1 μm be symbolized by the gain at 1030 nm. Thus we may write the following explicit equations:

$$\begin{aligned} \frac{G_{915}}{log_{10}(e)} &= -\alpha_{915} \cdot n_1 \\ \frac{G_{980}}{log_{10}(e)} &= g^*_{980} \cdot n_2 - \alpha_{980} \cdot n_1 \\ \frac{G_{1030}}{log_{10}(e)} &= g^*_{1030} \cdot n_2 \end{aligned} \tag{2.11}$$

From this linear set of equations, it is rather straightforward to show that the gain relations can be expressed in the simple form below.

$$G_{1030} = \frac{g^*_{1030}}{g^*_{980}} G_{980} + \frac{g^*_{1030}}{g^*_{980}} \cdot \frac{\alpha_{980}}{\alpha_{915}} G_{915} \tag{2.12}$$

If we now substitute the Giles parameters for the actual cross-sections and overlap factors, we obtain the final result for the gain relation (Eq. 2.13):

$$G_{1030} = \frac{\Gamma_{1030}}{\Gamma_{980}} \cdot \frac{\sigma^{em}_{1030}}{\sigma^{em}_{980}} G_{980} + \frac{\Gamma_{1030}}{\Gamma_{915}} \cdot \frac{\sigma^{em}_{1030}}{\sigma^{em}_{980}} \cdot \frac{\sigma^{abs}_{980}}{\sigma^{abs}_{915}} G_{915} \tag{2.13}$$

The superscripts on the cross-section factors indicate whether it is the absorption or emission cross-sections. For a double-clad fiber, the 1030 nm radiation and the 980 nm radiation will both propagate in the core and, since the their mode-fields will not differ substantially, the first factor of the first term can be crossed out. If we insert numerical values for the emission and absorption cross-sections, we get:

$$G_{1030} = 0.22 \cdot G_{980} + \frac{\Gamma_{1030}}{\Gamma_{915}} \cdot 0.7 \cdot G_{915} \tag{2.14}$$

Some interesting conclusions can be drawn from this relation. First of all, the contribution from the 980 nm gain is modest; assuming a cavity with 4 % reflectivity on the outcoupling side gives 96 % losses per roundtrip which corresponds to a necessary gain of ~14 dB per round trip or ~7 dB per single pass. This leaves a contribution of ~ 1.5 dB. The second term, specifically the first factor, can, on the other, hand have a serious effect on the parasitic gain in a double-clad fiber. To see this more clearly, let us assume that the optical modes for the pump (915 nm) and the signal (980 nm), respectively, have a flat-top beam profile. Then the overlap ratio reduces to the ratio of the core and cladding areas which can be substantial. The overlap ratio is generally referred to as the β factor [40, 50, 51]. The parasitic gain at 1030 nm has been plotted against the absorbed pump power at 915 nm for various β factors in Fig. 2.12.

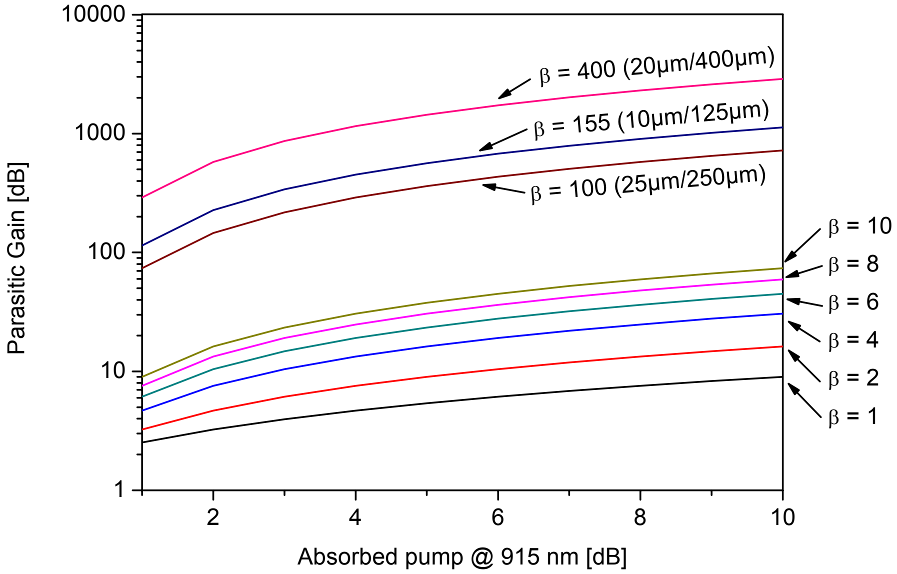

Fig. 2.12. Parasitic gain as a function of absorbed pump power for various β-factors.

It is evident that the β factor must be kept small as it is not possible to suppress more than perhaps 50 dB of gain at the parasitic wavelength before ASE will start to deplete the population inversion. This can, for example, be accomplished with a small core/cladding area ratio (with $\beta = 1$ for a core-pumped fiber). However, this is generally impractical in normal silica fibers as it is not possible to launch any substantial amount of pump from a diode laser into a core small enough to support a decent beam quality. Another approach is to use a PCF-fiber to maintain the beam quality even with large core sizes [50, 51]. A similar approach is to dump the unwanted ASE at 1030 nm by using a band-gap guiding PCF fiber [52]. For standard silica fibers, an interesting approach is instead to control the spatial doping profile, thereby changing the overlap ratio, e.g., ring-doping [40]. The general idea is to lower the factor Γ_{1030} without affecting the pump absorption. By placing the dopant in a ring on the edge of the core or even outside it, the optical mode in the core will interact more weakly with the dopant, allowing the population inversion to build up.

It is also of interest to look at the threshold pump power in this kind of laser. By requiring that the amplification in Eq. 2.2 is equal to one and by solving for the pump intensity in Eq. 2.6 with the signal intensity set equal to zero and, furthermore, by assuming no stimulated emission at the pump wavelength, it can be deduced that the necessary pump power needed to bleach the gain medium is given by the expression (Eq. 2.15):

$$I_{transp}^{915} = \frac{h \cdot \nu}{\tau} \cdot \frac{\sigma_a^{980}}{\sigma_a^{915} \cdot \sigma_e^{980}} \tag{2.15}$$

If we insert the numerical values from Section 2.3 into the equation above, it turns out that the minimum intensity to bleach an Yb-doped silica fiber at 980 nm emission is roughly 30 kW/cm^2. This implies that for single-pass pumping, a large cladding will invariably lead to large amounts of lost pump power. This is illustrated in Fig. 2.13 below where the threshold pump power has been calculated for a few different cladding diameters. The threshold is plotted against pump absorption which translates into the maximum fiber length that can be used.

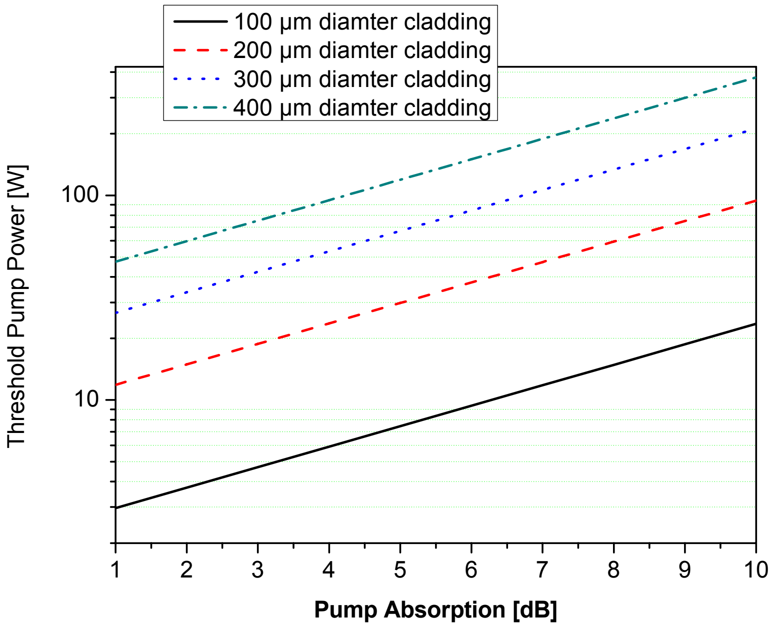

Fig. 2.13. Calculated threshold pump powers as a function of absorbed pump power at 915 nm for 4 cladding diameters.

2.6 Self-Pulsing

It has long been known that rare-earth doped fibers can exhibit strong temporal instabilities, i.e., self-pulsing. Self-pulsing can, if unchecked, cause catastrophic break-down in a fiber laser. When a pulse develops and thereby depletes the gain, it can have peak intensity several orders higher than the average intensity of the laser system. It is not uncommon for a pulse to reach peak powers above 10 GW/cm^2, which is close to the damage threshold of silica glass [53]. The main cause of these instabilities have been debated but it is believed to be related to the interaction between the laser signal and the population inversion [54]. Other factors such as stimulated Brillouin scattering (SBS) [55] and signal reabsorption in the weaker pumped part of the fiber [56] have also been associated with this phenomenon. There are techniques to mitigate this; decreasing the losses in the fiber (including outcoupling) should theoretically stabilize the system [57]. It has also been shown that increasing the length of the cavity to a degree where the photon life time is of the same order as the relaxation time of the upper laser level provides a stable system for all pump powers [58]. Furthermore, at high pump powers, the gain should theoretically replenish quickly enough to provide stable lasing [58, 59]. In Paper VI, we show that cooling part of the fiber gain medium down to liquid nitrogen temperatures efficiently suppresses self-pulsing. As the fiber is cooled down, the thermal population in the lower laser level will be removed. Signal reabsorption is, therefore, also effectively removed which inhibits self-pulsing [56]. This supports the theories which claim that saturable absorption is largely responsible for the onset of instabilities.

2.7 Photodarkening

Photodarkening is a color-center related effect that appears in Yb-doped silica fiber when subjected to strong radiation close to the resonance lines of the Yb-ion. Although the effect is reversible through heating of the fiber [60] or by irradiation with UV light [61], it will reduce the efficiency of a laser system as it induces an unsaturable loss. The photodarkening rate depends strongly on the density of excited Yb-ions (a power-law dependence of the 7th order of the Yb-concentration has been shown [62]) which means that it can be reduced by lowering the concentration in the fiber and by operating the laser at wavelengths far above 1 μm. It has also been shown that codoping with phosphorus (P) will mitigate the effects of photodarkening [63] but this brings in other detrimental effects such as reduced cross-sections and an increased background loss. In Paper VII, we show that cerium (Ce) codoping mitigates the effect without the detrimental effects found with P-codoping. A more detailed discussion of this if found in Chapter 4.

3 Volume Bragg Gratings

It was discussed in Chapter 2 how spectral control could be achieved in solid-state lasers, specifically fiber lasers. Both FBGs and surface gratings have their uses in many applications but, in several cases involving speciality fibers for high power applications, VBGs offer many advantages. In this chapter a short background to VBGs will be given.

3.1 PTR-Glass Properties

VBGs are generally fabricated using photothermorefractive (PTR) glass. This inorganic photosensitive glass was first discovered in the 1940s in the former Soviet Union, but it was not until the 1990s that it was first used to record Bragg structures [64, 65]. The glass itself is based on lithium-aluminum-silicate or sodium-zinc-aluminum-silicate glass [65] doped with silver (Ag) and cerium (Ce). By exposing the glass to UV radiation close to the Ce absorption band centered at 305 nm, the Ce-ions photoionize through the process $Ce^{3+} \rightarrow Ce^{4+} + e^{-}$, leaving a free electron. The electron can then be captured by the Ag-ion through the process $Ag^{+} + e^{-} \rightarrow Ag^{0}$. In the next step, the glass is heated to ~500 ˚C where two things happen: through the diffusion of Ag in the glass, tiny silver crystals are formed in the exposed regions. These Ag-crystals will, in-turn, serve as nucleation centers for NaF-crystals. It is primarily the formation of these NaF-crystals which is responsible for the spatial modulation of the refractive index as it is lowered at the sites of the NaF-crystals. The maximum reported modulation strength is $\Delta n = 1.2 \times 10^{-3}$ (2008) [66], but Δn is generally on the order of $\sim 10^{-4}$.

The transmission widow of unexposed PTR-glass, i.e., where the absorption losses are below 0.1 cm^{-1} [64], lies between 550 nm and 2800 nm. After processing, the main loss mechanism within this transmission window is scattering, which is believed to come from the formation process of the NaF-crystals. This loss depends strongly on wavelength, composition, annealing and UV exposure time [67], but it is normally below 0.01 cm^{-1} for transmission in the 1 μm region [68]. Other properties of importance for laser applications are the thermal expansion and the thermo-optic coefficients, which have been reported to have the values $\alpha = 8.4 ppm / K$ [69] and $dn / dT = 0.05 ppm / K$ [70], respectively. These properties influence the stability of the grating since thermally induced variations in stress and refractive index can distort the Bragg structure [71-73]. This topic is handled separately later in the chapter.

3.2 Plane Wave Theory

Much of the theoretical work performed on Bragg gratings stems from the work of Kogelnik in 1969 [74]. The theory is based on a plane-wave approximation meaning that the incident electric field only varies in the direction of propagation. In this section, the reflection and transmission coefficients for a Bragg grating are derived using coupled-wave theory. In this derivation, we assume that we are at normal incidence at a Bragg grating with an incident electric field with subscript M and a reflected electric field with subscript N. Furthermore, the grating has a periodic index modulation with grating period Λ and a length d. The Bragg condition in momentum space is thus defined as:

$$\bar{k}_N = \bar{k}_M - \bar{K} + 2\bar{\delta} \tag{3.1}$$

In Eq. 3.1 above, $\bar{k}_{N,M}$ are the wave-vectors for the incident and reflected electric fields M and N, respectively. $\bar{K}$ is the grating vector and $\bar{\delta}$ is the wave-vector mismatch, which has been included to allow for non-perfect phase matching. The grating and the Bragg condition are illustrated in Fig. 3.1 (a) and (b), respectively.

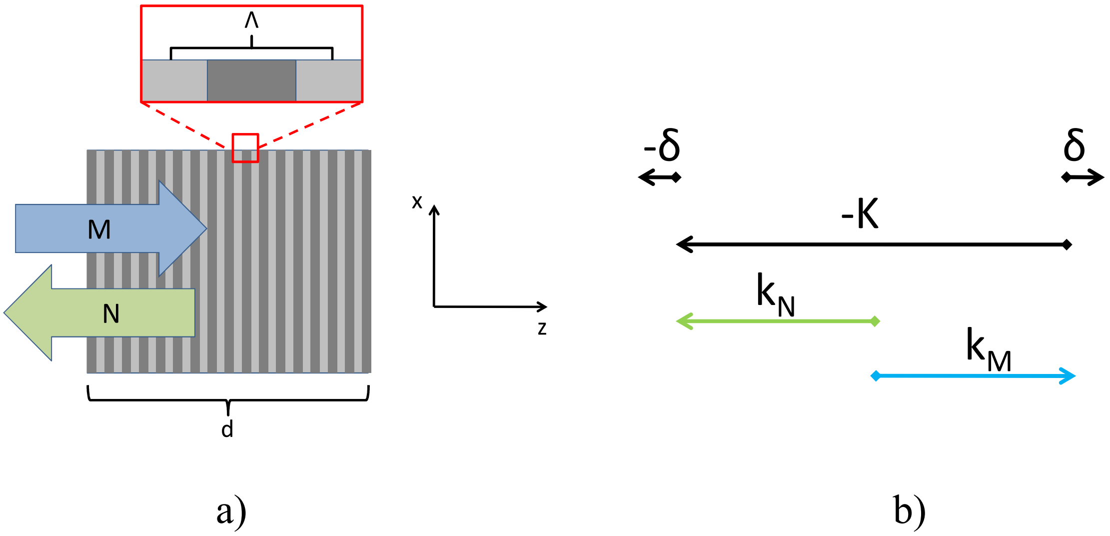

Fig. 3.1. a) Illustration of the Bragg structure in a VBG. b) The Bragg condition in k-space.

As the wavelength must be the same for the incident and the reflected light, we can express $k_{N,M} = 2\pi n_0 / \lambda \equiv \beta$. Furthermore, the grating vector can be expressed as the reciprocal lattice vector with an amplitude $|\bar{K}| = 2\pi/\Lambda$. In the event that we have perfect phase matching ($\delta = 0$), Eq. 3.1 reduces to

$$\begin{aligned} -\beta \cdot \bar{e}_z &= \beta \cdot \bar{e}_z - K \cdot \bar{e}_z \\ \Rightarrow \lambda_B &= 2n_0 \Lambda \end{aligned} \tag{3.2}$$

The last expression in Eq. 3.2 is the well-known Bragg condition for normal incidence with λ_B being the Bragg wavelength. Of equal interest are the transmission and reflection coefficients for the incident electric field. To determine these we assume that the light is polarized along the y-axis, orthogonal to the plane of incidence. Furthermore, we assume that the grating modulation can be written as $n(z) = n_0 + n_1 \cdot f(z)$ where n_0 is the average refractive index and n_1 is the modulation strength of the grating. The wave equation can then be written as

$$\left(\frac{d^2}{dz^2} + \beta^2 + 4\beta\kappa f(z) \right) E(z) = 0 \tag{3.3}$$

In Eq. 3.3 above, $\kappa = \pi n_1 / \lambda$ is the coupling strength and $E(z)$ is the total electric field inside the grating. The grating can, of course, have any arbitrary modulation, but it is here assumed that it has a sinusoidal variation. This also means that the Fourier expansion of $f(z)$ only has two non-zero coefficients:

$$f(z) = sin(Kz) = \frac{1}{2i}\left(e^{iKz} - e^{-iKz} \right) \tag{3.4}$$

The electric field inside the grating can now be written as the sum of the incident and the reflected fields:

$$E(z) = M(z) + N(z) = \tilde{M}(z) \cdot e^{-ik_M z} + \tilde{N}(z) \cdot e^{ik_N z} \tag{3.5}$$

Where $\tilde{M}$ and $\tilde{N}$ are the incident and reflected field amplitudes, respectively. With only light incident from the negative z direction, the boundary condition becomes:

$$\begin{aligned} \tilde{M}(0) &= M_0 \\ \tilde{N}(d) &= 0 \end{aligned} \tag{3.6}$$

Inserting the electric field from Eq. 3.5 into Eq. 3.3 and employing the slowly varying envelope approximation (SVEA), we can neglect the second-order derivatives. Furthermore, if we let all fast oscillating terms average to zero and collect all the terms with the same exponent, we finally arrive at the coupled-wave equations:

$$\begin{aligned} \frac{d\bar{M}}{dz} &= i\delta\bar{M} + \kappa\bar{N} \\ \frac{d\bar{N}}{dz} &= \kappa\bar{M} - i\delta\bar{N} \end{aligned} \tag{3.7}$$

In the expressions above, a change of variables was carried out for the field amplitudes, such that $\tilde{M} = \bar{M} \cdot e^{-i\delta z}$ and $\tilde{N} = \bar{N} \cdot e^{i\delta z}$. The eigenvalues, $\gamma = \pm\sqrt{\kappa^2 - \delta^2}$, and the eigenvectors, $(\pm\gamma + i\delta, \kappa)$, of Eq. 3.7 give the solution to the electric fields inside the grating as follows:

$$\begin{aligned} M(\delta, z) &= M_0 t(\delta, z) e^{-i(k_M + \delta)z} \\ N(\delta, z) &= M_0 r(\delta, z) e^{i(k_N + \delta)z} \end{aligned} \tag{3.8}$$

In the solutions above, the transmission and reflection coefficients $t(\delta, z)$ and $r(\delta, z)$, are given by:

$$\begin{aligned} t(\delta, z) &= \frac{-\gamma \cosh\left(\gamma(d - z)\right) + i\delta \sinh\left(\gamma(d - z)\right)}{-\gamma \cosh\left(\gamma d\right) + i\delta \sinh\left(\gamma d\right)} \\ r(\delta, z) &= \frac{\kappa \sinh\left(\gamma(d - z)\right)}{-\gamma \cosh\left(\gamma d\right) + i\delta \sinh\left(\gamma d\right)} \end{aligned} \tag{3.9}$$

From Eq. 3.8 and Eq. 3.9 we can finally obtain an expression for the total fraction of reflected power:

$$R(\delta) = \left| \frac{N(\delta, 0)}{M(\delta, 0)} \right|^2 = \left| r(\delta, 0) \right|^2 = \frac{\kappa^2 \sinh^2\left(\sqrt{\kappa^2 - \delta^2} \cdot d\right)}{\kappa^2 \cosh^2\left(\sqrt{\kappa^2 - \delta^2} \cdot d\right) - \delta^2} \tag{3.10}$$

From the expression above, it is evident that the maximum reflectivity, Rmax, is obtained for $\delta = 0$. Eq. 3.10 can then be rewritten as:

$$R_{max} = \tanh^2\left(\kappa d\right) \tag{3.11}$$

In this expression, it is clear why κ is called the coupling strength. Another important factor is the spectral bandwidth of the grating. This can be defined in several ways; here we choose to define the bandwidth as the spectral distance between the two zeroes closest to the peak. These are located at $\delta = \pm\sqrt{\kappa^2 + \pi^2 / d^2}$, respectively, which, together with Eq. 3.1, gives the total spectral bandwidth as:

$$\Delta\lambda_B = \lambda_B \sqrt{\left(\frac{n_1}{n_0}\right)^2 + \left(\frac{2\Lambda}{d}\right)^2} \tag{3.12}$$

From Eqs. 3.11 and 3.12, we can see that the combination of high reflectivity and broad bandwidth can be difficult to obtain at the same time since a shorter VBG for larger $\Delta\lambda_B$ requires a larger n_1. Furthermore, this increases the scattering losses as the fraction of NaF-crystals is increased with increasing n_1. The properties of Bragg wavelength, max reflectivity and bandwidth are illustrated in Fig. 3.2 for the grating used in Paper V.

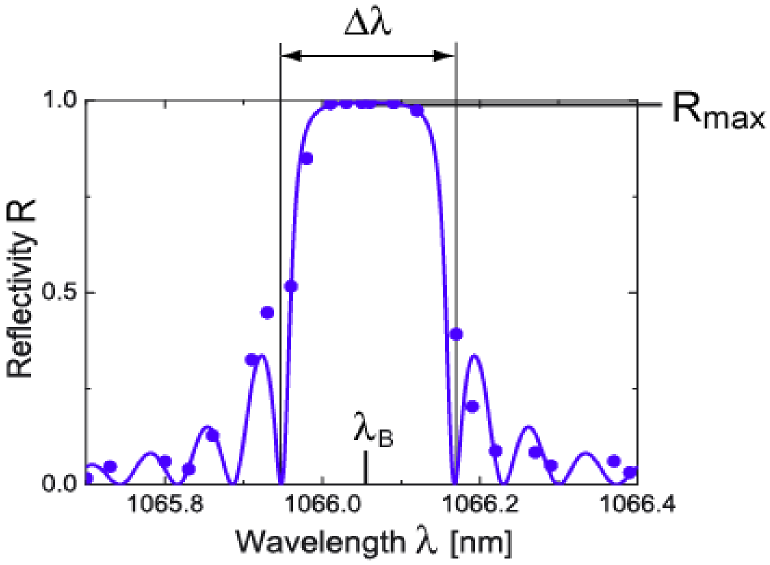

Fig. 3.2. Peak reflectivity, Bragg wavelength and bandwidth of a grating in the plane-wave approximation. The dots correspond to measured reflectivity for different wavelengths (Image courtesy of B. Jacobsson [75]).

3.3 Tuning Characteristics

The reflection peak of a Bragg grating, λ_B, can be tuned to other wavelengths by heating or cooling the grating. The effect is clearly seen if we differentiate the Bragg condition in Eq. 3.2 with respect to temperature:

$$\begin{aligned}\frac{d\lambda_B}{dT} &= \frac{d}{dT}\left(2n_0\Lambda\right) = 2\frac{dn_0}{dT}\Lambda + 2n_0\frac{d\Lambda}{dT} \\ &= \left\{\alpha = \frac{1}{\Lambda}\frac{d\Lambda}{dT}\right\} = \lambda_B\left(\frac{1}{n_0}\frac{dn_0}{dT} + \alpha\right)\end{aligned} \tag{3.13}$$

Here, α is the thermal expansion coefficient. From the properties of the PTR-glass, we know that $\alpha = 8.4 ppm/K$ and $dn/dT = 0.05 ppm/K$. It is, therefore, evident that the main contribution to the thermal tuning strength comes from the thermal expansion coefficient and one can generally expect a tuning rate of $d\lambda_B/dT \approx 10 pm/K$ for 1 µm radiation. Even though the thermal tuning range is rather limited, the high degree of control can be very useful when matching the Bragg wavelength to that of a resonance line of a rare-earth ion or to another grating.

A more powerful tuning method is angle-tuning. By rotating the grating, the Bragg wavelength will shift as the perceived grating period changes. The Bragg condition then becomes:

$$\lambda_B = 2n_0\Lambda\cdot\cos(\theta) \tag{3.14}$$

Here, θ is the angle between the incident radiation and the grating normal. The derivation in the previous section can now easily be extended to include oblique incidence, and the expressions for the maximum reflectivity and the bandwidth are still valid if we perform the simple substitution of variable: $\kappa' = \kappa/\cos(\theta)$. If the grating is to be used in a laser resonator where continuous tuning is wanted, the cavity needs to be realigned every time the grating is adjusted. The problem is illustrated in Fig. 3.3. This can be resolved by placing the grating in a retroreflector configuration [76] as illustrated in Fig. 3.4. This ensures that all of the light is reflected back in a direction parallel to the incoming light, regardless of the tuning angle. As can be seen in the figure, the reflected light will, however, be offset by some distance compared to the incoming light, but this is easily handled by a second mirror (not shown), orthogonal to the direction of propagation. With this construction, the tuning range is limited only by the aperture of the grating.

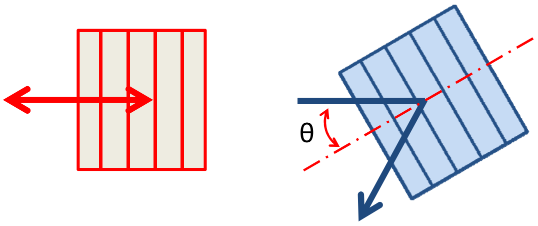

Fig. 3.3. Light reflected in a VBG from normal incidence (left) and oblique incidence (right).

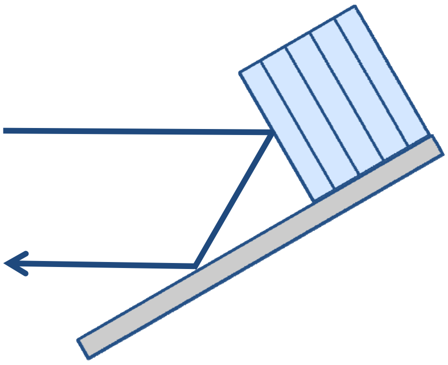

Fig. 3.4. VBG in retro-reflector configuration. The reflected beam is anti-parallel to the incident beam.

In the plane-wave approximation, for small rotation angles, there is no major change in the peak reflectivity. Unfortunately, the approximation breaks down for large angles, narrow beam waists inside the grating, and/or less than diffraction-limited beams [77]. For the plane-wave approximation to be valid at normal incidence, the following inequality must hold [77]:

$$\left(\frac{\pi}{2}\right)^2 \cdot n_0^2 \left(\frac{\omega_{e^{-2}}}{\lambda_B}\right)^2 \cdot \frac{\Delta\lambda_B}{\lambda_B} > 1 \tag{3.15}$$

For oblique incidence, the inequality becomes:

$$\frac{\pi}{4} \cdot n_0 \frac{\omega_{e^{-2}}}{\lambda_B} \cdot \frac{\Delta\lambda_B}{\lambda_B} > \sin(\theta) \tag{3.16}$$

In Eq. 3.15 and Eq. 3.16 above, $\omega_{e^{-2}}$ is the e^{-2} intensity beam radius (spot-size). From Eq. 3.16, it can be seen that the beam radius here is much more crucial as the inequality depends linearly on beam radius/wavelength ratio (compared to the square dependence in Eq. 3.15). It is also evident that the maximum tuning angle increases with a larger grating bandwidth. Eq. 3.15 and 3.16 are easily expanded to accommodate for less-than-diffraction-limited beams by the variable substitution: $\omega_0 \to \omega^* / M^2$, where ω^* is the beam radius incident on the VBG and M^2 is the beam parameter product [78]. It turns out that the tuning range is quickly reduced with decreasing beam quality and the VBG instead starts to act as a spatial filter. The angular tuning limitations are illustrated in Fig. 3.5 below for a VBG with a Bragg wavelength of 1066 nm, a bandwidth of 0.4 nm, and with an incident beam with three different M^2 values: 1, 2 and 5, respectively:

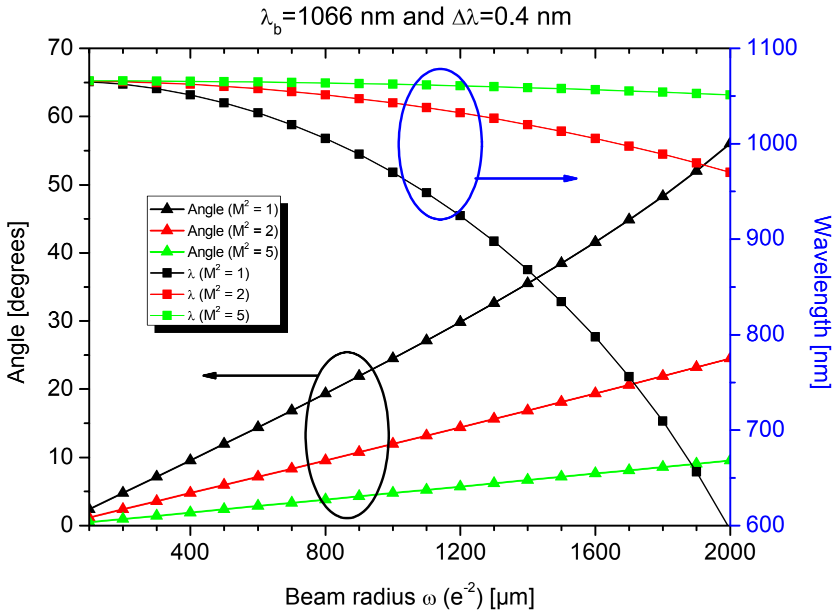

Fig. 3.5. Maximum tuning angle and wavelength tuning limit for a VBG with design wavelength 1066 nm and bandwidth 0.4 nm.

3.4 Thermal Limitations

The normalized averaged intensity variation inside a VBG along the optical axis is given by the following expression [74]:

$$I(z) = \frac{1}{\cosh\left[\tanh^{-1}\left(\sqrt{R}\right)\right]} \cdot \cosh\left[2 \cdot \tanh^{-1}\left(\sqrt{R}\right) \cdot (d - z)\right] \qquad (3.17)$$

As before, *R* is here the reflectivity of the VBG, *z* is the distance along the optical axis into the VBG, and *d* is the length of the VBG. It can be seen in Eq. 3.17 that the intensity variation depends strongly on the diffraction strength. If we assume a VBG length of 5 mm, as this corresponds to most of the gratings used in this thesis, we can plot the total intensity for different positions inside the VBG along the optical axis for various reflectivities (see Fig. 3.6).

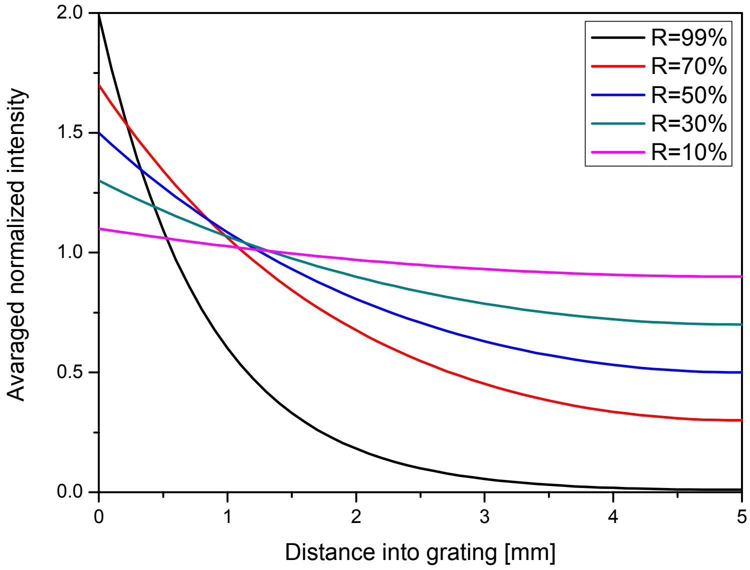

Fig. 3.6. Sum of normalized incident and reflected intensity along the optical axis (z) in a 5 mm long VBG for various reflectivities.

Even though the absorption is low in PTR-glass, it is conceivable that a beam with a high enough power incident on the VBG could create a thermal gradient. This would then change the Bragg condition as can be seen in Eq. 3.13. As an example, if we let a 1 kW gaussian beam with a radius of 1 mm enter a VBG with an circular aperture of 3 mm (the same as was used in Paper V) and assume a modest absorption of 10^{-3} cm^{-1}, we can numerically simulate the thermal distribution in the VBG. The result is plotted in Fig. 3.7 below. The VBG boundaries are set to a fixed temperature of 300 K, mimicking the placement in the temperature-controlled holder and it is assumed that the front and back side are cooled by convection.

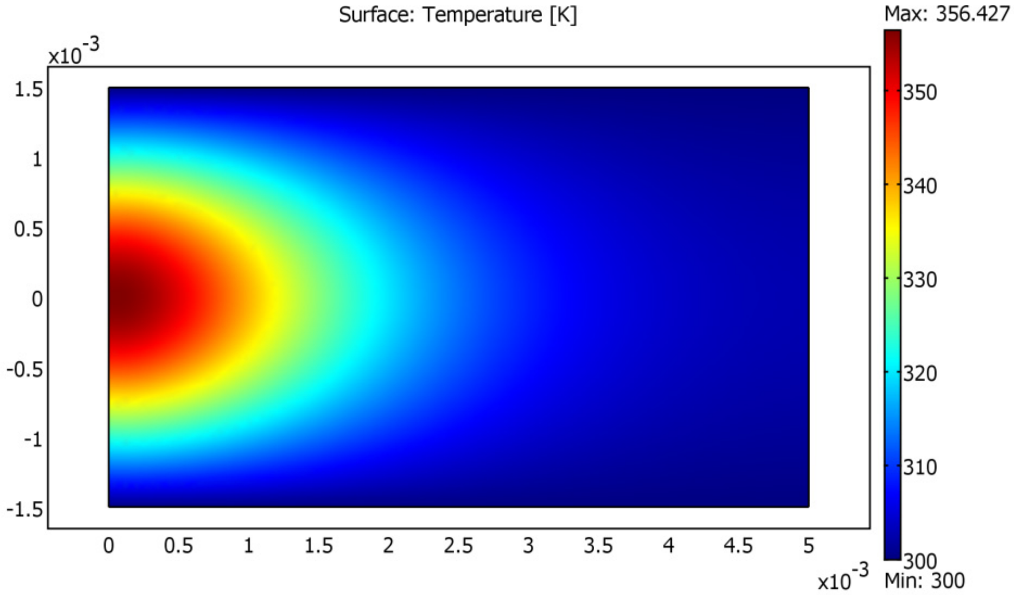

Fig. 3.7. Simulated temperature distribution in a highly reflective VBG subjected to a 1 kW beam with a beam radius of 1 mm and assuming an absorption of 10^{-3} cm^{-1}. The image shows the cross-section along the VBG (x-axis is distance into VBG).

This shows that we can expect a temperature drop along the propagation axis of the VBG of ~55 K, corresponding to a shift in the peak reflectivity wavelength of almost ~0.5 nm. A high-intensity narrow-linewidth beam would thus get partially transmitted as the temperature gradient builds up. In a low-gain resonator, the power oscillating inside the cavity must be kept high, implying that a high finesse is important. A thermal chirp in the grating could thus severely limit the performance. This is generally speaking not a problem in fiber lasers as the high gain make the system less susceptible to small changes in the end-reflectors (see Chapter 2). Furthermore, the intensity at the end-reflectors in a fiber laser can differ substantially. If the beam incident on the VBG is ~1 kW, the output of the fiber laser would be maybe 5 times higher, that is ~5 kW, in which case other thermal effects would become important [79]. If we, on the contrary, assume a more reasonable output power of 1 kW, the intra-cavity power incident on the VBG would be around ~200 W. For the same simulation data, this would correspond to a temperature gradient inside the VBG of ~5 K.

3.5 Alignment Techniques

Alignment of VBGs differs a great deal from the highly reflective mirrors normally used in laser cavities as there is no feedback at the design wavelength of the VBG until it is aligned. Furthermore, the Bragg planes are intentionally offset from the specular reflection in order to avoid broadband parasitic feedback. While brute-force alignment is always possible, it is very tedious and time consuming. Two techniques were therefore developed here to take advantage of the emission properties associated with fiber lasers and provide a quicker and easier alignment. The first technique works well with narrow bandwidth gratings and uses the spectral filtering properties of the VBG to identify which direction the grating should be rotated in order to align it. An optical spectrum analyzer is placed on the rear side of the VBG where the fluorescence of the fiber is collected. A dip in the spectrum will now show for which wavelength the grating is aligned and, as the grating is rotated, the dip will move to longer or shorter wavelengths depending on whether the grating is rotated towards or away from alignment, respectively. The longest wavelength that can be reflected is of course the design wavelength of the grating for normal incidence. This is illustrated in Fig. 3.8 below. The dotted line (blue) shows the emission spectrum just before alignment and the solid curve (red) shows the spectrum when the grating is aligned with the optical axis.

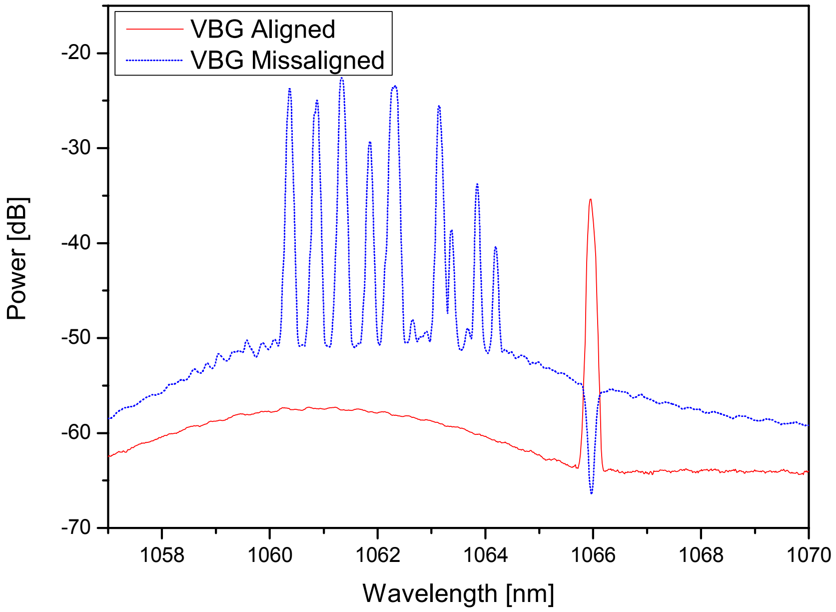

Fig. 3.8. Spectral emission through the VBG during alignment: Dotted line (blue) shows the emission just before alignment, solid line (red) shows the emission just after alignment.

For gratings with a large bandwidth, it can be difficult to resolve how the dip in the emission spectrum is moving when the VBG is close to alignment. Furthermore, if the grating wavelength is located far outside the fluorescence peak of the fiber, it can also be difficult to resolve the dip as it may be of the same strength as the noise. The signal can, of course, be integrated over a long enough time period to reduce the noise but this will again make the alignment very time consuming and frustrating.

The second method is somewhat more complicated but produces more consistent results in both of these described situations. The idea is essentially to map the Bragg planes to the surface of the VBG which only requires that fluorescence (or any light source propagating in the fiber) is available at shorter wavelengths than the design wavelength. The concept is illustrated in Fig. 3.9 below. The fluorescence (green line) is coupled through an aperture before entering the VBG. As the VBG is rotated, certain angles will match the Bragg condition for the fluorescence peak which then can be marked on the aperture as illustrated with the dashed circle. At the same time, a visible laser such as a HeNe (red line) is launched through a second aperture onto any of the other sides of the VBG. For each reflected fluorescence peak, a corresponding mark will be made where the HeNe is reflected on the second aperture. This is repeated for as many points as necessary until two circles have been traced out on the two apertures. While the fluorescence circle (green) will be centered on the aperture, the HeNe circle (red) will, in general, be offset bysome amount. The VBG can now easily and repeatedly be aligned by rotating it in such a way that the reflected HeNe peak hits the center of the traced-out HeNe circle.

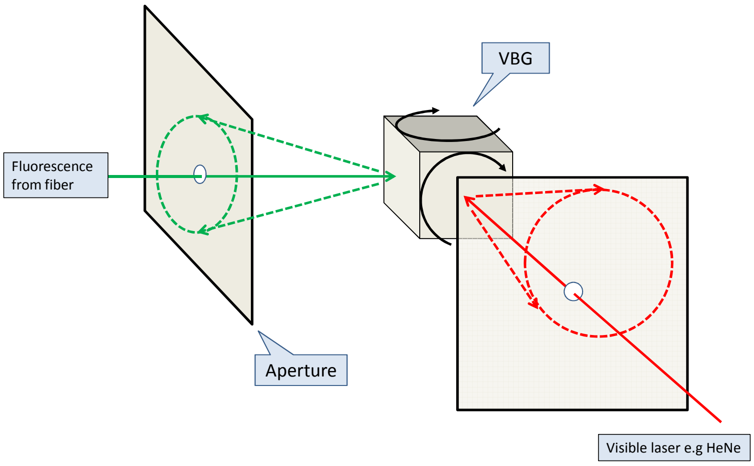

Fig. 3.9. Illustration of alignment method of VBG. The method is based on mapping an arbitrary surface of the VBG to the Bragg planes.

4 Fiber Laser Experiments

4.1 Nd-doped Micro Structured Fiber Laser

In a proof of concept experiment (Paper I), we showed how VBG could be used in a fiber laser employing a fiber type which traditionally is difficult to lock with FBGs. The fiber was of a type known as a leaky channels fiber which has attracted a great deal of interest in the last couple of years as they allow large core areas while still maintaining essentially single-mode operation. The reason for this is that although the core theoretically can support many transverse modes, the structure of the fiber induces high losses for higher order modes. In our case, the fiber had a neodymium (Nd) doped core (1300 ppm) which was surrounded by five air holes with a diameter of 18 μm and a pitch of 19 μm [80]. The core itself had a diameter of ~18 μm and a NA of 0.156 which gives a V-number of roughly 18 and typically would support a large number of higher order modes. A cross-section of the fiber is shown in Fig. 4.1.

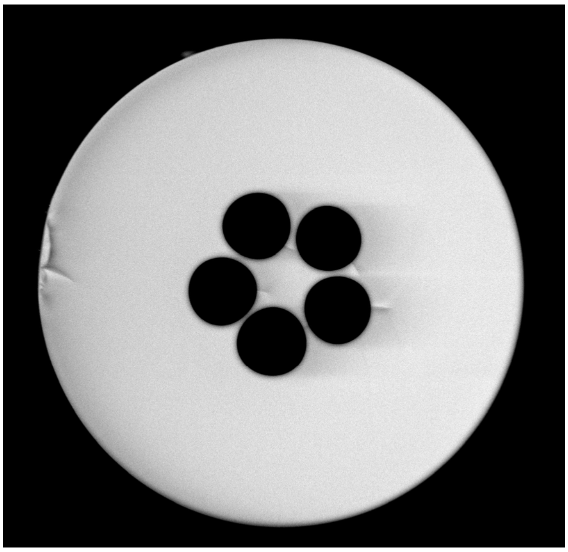

Fig. 4.1. Cross-section of microstructured Nd-doped fiber.

Due to the air holes, it was not possible to cladding pump the fiber which meant that the pump light had to be launched into the core directly. A Ti:Sapphire laser was therefore used as a pump source even though the pump power was somewhat limited (~700 mW) . A simple setup was constructed (see Fig. 4.2)) where the VBG was placed at the rear end of the fiber while the fiber facet on the front provided outcoupling with only Fresnel reflections as feedback.

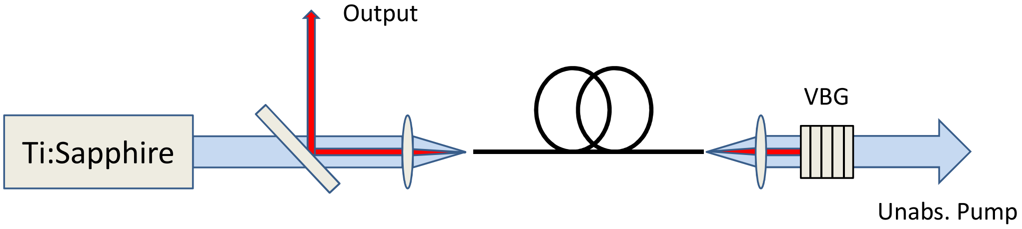

Fig. 4.2. Schematic illustration of the Nd-doped microstructured fiber laser.

The VBG used in this experiment had a high diffraction strength with a reflectivity of 99 % with an aperture of 5x2 mm and a length of 5 mm which corresponds to a bandwidth of ~0.2 nm. The grating was AR-coated for 1 μm radiation and was angle polished to prevent parasitic reflections from interfering with the cavity. The output power, slope efficiency and spectral characteristics were compared between the VBG and a dielectric highly reflective mirror. As can be seen in Fig. 4.3, the behavior with the two reflectors was very similar. A slight difference in threshold was found, 103 mW compared to 101 mW of launched pump power, as well as maximum output power, 166 mW compared to 188 mW for the VBG and mirror, respectively. The corresponding slope efficiencies were 51 % for the VBG and 57 % for the mirror.

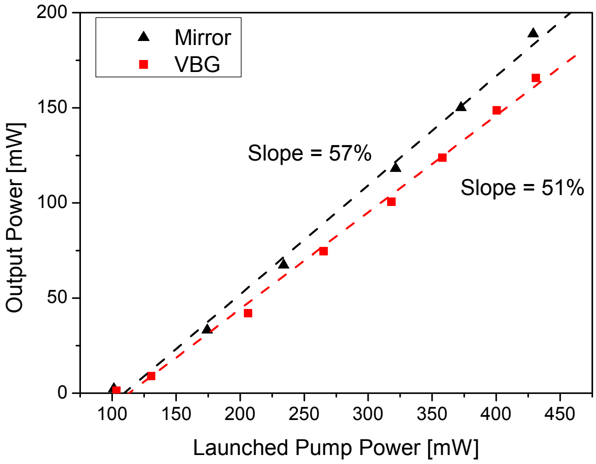

Fig. 4.3. Slope efficiency comparison for VBG and mirror based Nd-doped fiber laser.

The emission linewidth was ~7 nm wide with the mirror setup which is to be expected from a free running fiber laser as the mode spacing is very small (in this case on the order of

100 MHz) and the gain region is large. With the VBG, the emission was not only contained within the bandwidth of the VBG but was below the resolution limit of the optical spectrum analyzer used (< 0.07 nm). Both emission spectrums are plotted in Fig. 4.4.

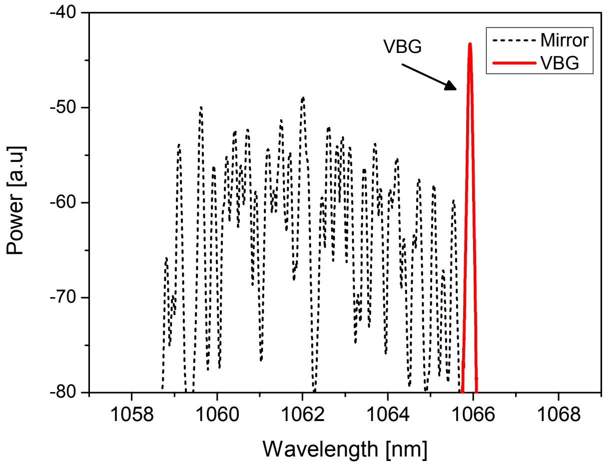

Fig. 4.4. Comparison of spectral emission for VBG and mirror based Nd-doped fiber laser.

Finally, the beam quality was measured to determine how close the fiber laser operated to a single transverse mode. As can be seen in Fig. 4.5, the output beam had an M^2 value of less than 1.6, meaning that the laser emission was close to diffraction limited. The results showed that VBGs are a very attractive alternative for wavelength locking and frequency stabilization of fiber lasers where FBGs are not easily integratable. Furthermore, the free space design opens up possibilities for insertion of other bulk components, such as acousto-optic modulators, optical isolators etc. This was also the first ever VBG locked fiber laser.

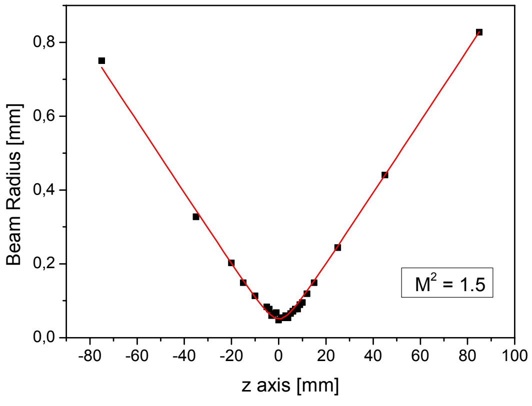

Fig. 4.5. Beam quality measurement of Nd-doped fiber laser.

4.2 Tunable Fiber Lasers

Based on these positive results (Paper I), a new experiment was designed (Paper II), but this time with a large-mode area Yb-doped fiber that was slightly multi mode. Yb-based fibers are a very attractive gain medium due to their simple energy structure and the high efficiency possible. The fiber used here had a core and cladding diameter of 30 µm and 250 µm with corresponding NAs of 0.07 and 0.46, respectively. With a the large area high NA cladding, the pump source in this experiment was a medium power fiber coupled laser diode emitting at 980 nm. The goal of the experiment was to determine how well a VBG could tune the emission linewidth within the large gain region of Yb-doped silica. However, as the fiber was pumped close to 980 nm and emission is possible down to below 1 µm, separating the pump and the signal would be a problem. A new pumping technique was therefore invented where the difference in core and cladding NA was used for pump and signal separation. The principle is illustrated below in Fig. 4.6.

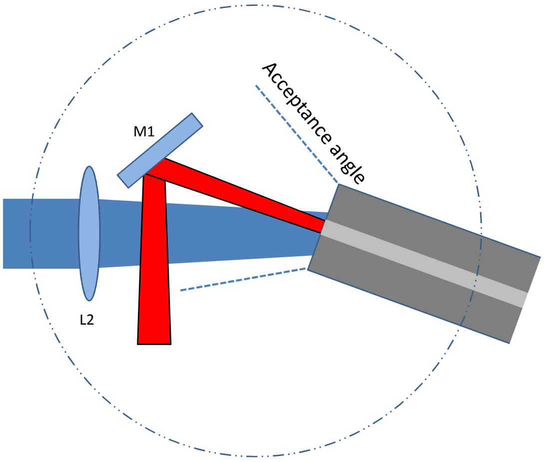

Fig. 4.6. Illustration of skew-angle pumping method for separation of pump and signal.

As the pump delivery fiber had a better beam quality than what was necessary to stay within the acceptance angle limit the cladding, the launch angle and spot size could be varied. By launching the pump light at a slight angle while still making sure that no part of the converging beam is outside the acceptance angle of the cladding, a high launch efficiency is still achieved. When lasing starts, the signal will exit the fiber under a smaller angle than the pump light enters due to a much smaller NA. After a short distance, the pump and signal beams will be spatially separated. The dimensions in Fig. 4.6 has been exaggerated for clarity, the actual setup is shown in Fig. 4.7.

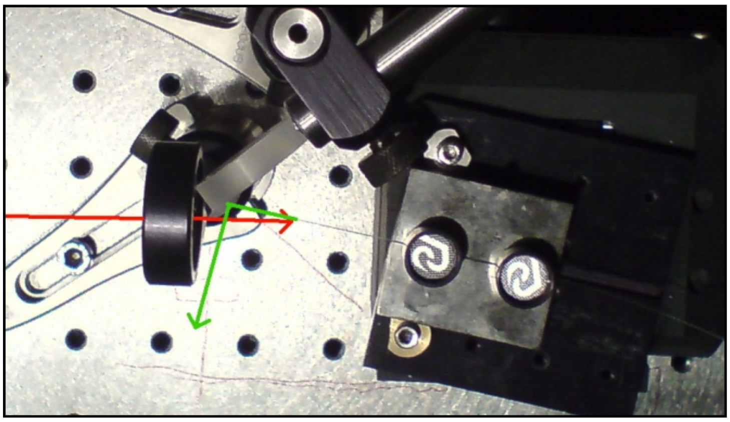

Fig. 4.7. Actual experimental setup employing skew-angle pumping.

The complete experimental setup is illustrated below in Fig. 4.8. The end facet on the pump side of the fiber acted as output coupler with a 4 % Fresnel reflection. The VBG was placed at the rear end of the fiber in a retro-reflector configuration as explained in Chapter 3, to allow efficient and continuous tuning.

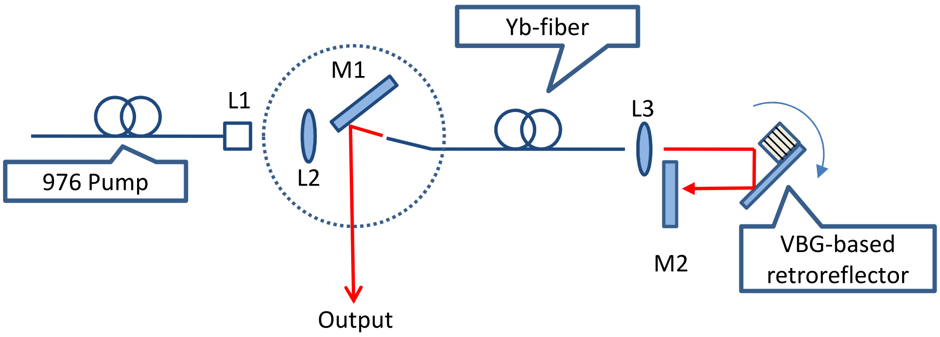

Fig. 4.8. Experimental setup showing an Yb-doped fiber laser with tunable VBG-based retro-reflector. A detailed illustration of skew-angle pumping (dotted circle) is found in Fig. 4.6.

With this setup, a continuous tuning from 1022 nm to 1055 nm was possible without parasitic lasing taking place. Below 1022 nm, parasitic lasing from the end faces of the fiber limited the efficiency, even though tuning down to 1015 nm was possible. The upper tuning range was limited by the length of the right angled mirror attached to the VBG. Throughout the tuning range, a high slope efficiency (~ 77 %) was recorded with a maximum output power of 5.5 W at 1035 nm. Output power and emission spectra is shown in Fig. 4.9 and Fig. 4.10, respectively.

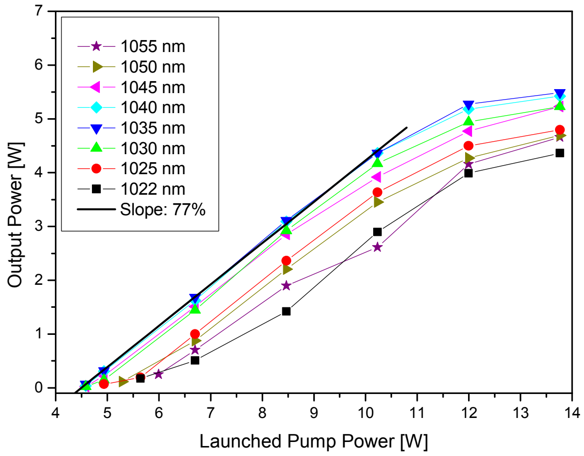

Fig. 4.9. Slope efficiency for several wavelengths covering the tuning range.

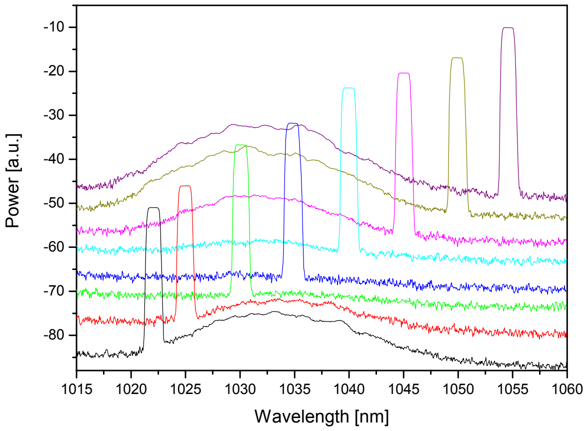

Fig. 4.10. Emission spectrum for the same wavelengths as above in Fig. 4.9. The emission spectrums were recorded with a resolution of 1 nm. The emission linewidth was in reality ~5 GHz.

In the previous experiment with the Nd-doped fiber, the microstructured design provided losses for the higher order transverse mode, which facilitated a good beam quality. In this experiment however, tight coiling was used to suppress transverse multi mode operation. With a V-number of ~ 6, the core supported roughly 20 modes at 1030 nm. By coiling the fiber, the losses for higher order modes can be increased [81] at the same time as an increased pump absorption is obtained [82]. Normal spool coiling was investigated but it was found that even at a coil radius of 2 cm, the higher order mode losses were too low to suppress multi mode oscillations. However, by coiling the fiber on two spools at right angles [15], the symmetry of the waveguide could be reduced even further and close to single transverse mode operation was possible. This was verified using a knife edge technique and it was found that the laser emission had an M^2 value of less than 1.3. The result is shown below in Fig. 4.11.

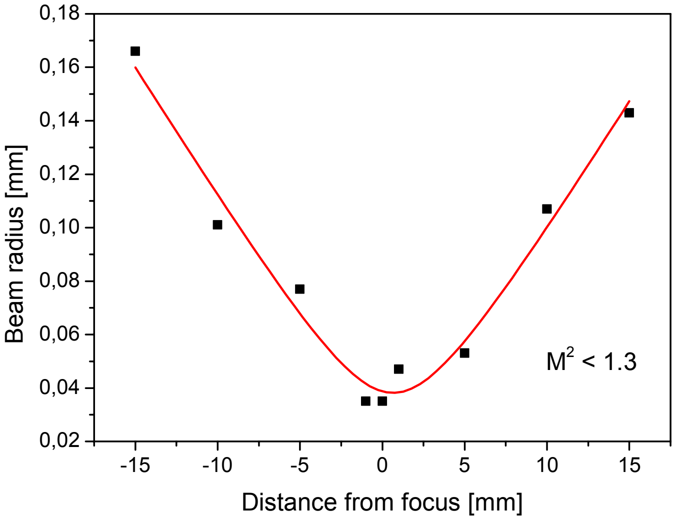

Fig. 4.11. Beam quality measurement for the coiled tunable Yb-doped fiber laser.

As the linewidth was again below the resolution of our optical spectrum analyzer, a scanning Fabry-Perot interferometer was used to measure the actual linewidth. It was found to be ~5 GHz which is considerably smaller than the bandwidth of the VBG, which was 146 GHz. The narrow linewidth can be explained by that the VBG bandwidth does not have a top-hat profile as was shown in Chapter 3 and the reflectivity is consequently higher in the center of the grating. The wavelength exactly matching the peak reflectivity will thus have a lower threshold.

The experiment thus showed that it was possible to cover a substantial part of the Yb gain region with maintained efficiency and linewidth. The simplicity and compactness of the arrangement is highly attractive as it allows continuous realignment free tuning.

4.3 High Out-Coupling Narrow Band Fiber Lasers

In the previous two experiments, a single VBG was used to narrow the linewidth of the two fiber lasers. This meant that the feedback from the other cavity end came from the fiber end face and was broadband. An experiment was therefore setup to show how two standard highly reflective VBGs could be used to achieve a narrow linewidth with maintained output power and efficiency and with the added possibility to dynamically adjust the reflectivity of the outcoupling (Paper III). The experimental setup is shown below in Fig. 4.12. The gain fiber was an Yb-doped fiber with 20 µm diameter core and 400 µm diameter cladding. With a NA of 0.06 for the core, the output was close to diffraction limited. Both fiber ends were angle polished to reduce parasitic reflections and make sure that the cavity was defined by the VBGs only.

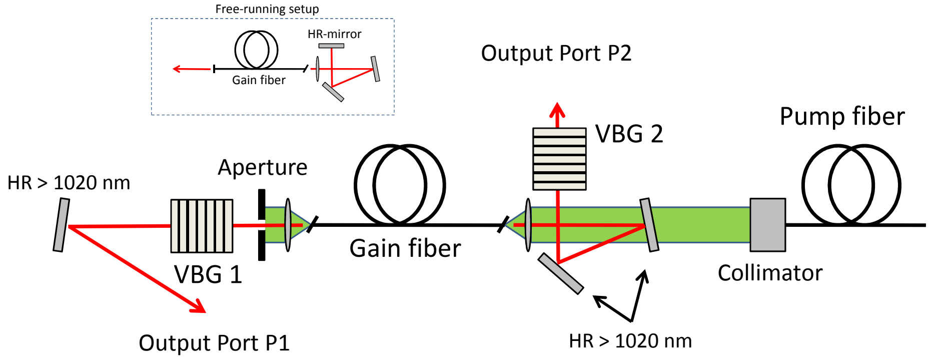

Fig. 4.12. Schematic illustration of the dual-VBG setup.

The two VBGs designated VBG1 and VBG2 were close to identical with respect to peak reflectivity (99% at 1065.9 nm) and bandwidth (0.22 nm), as they were cut from the same original sample. The gratings were angle polished and AR-coated to reduce parasitic reflections. The temperatures of the two VBGs were controlled with Peltier elements and could be set from 15 ˚C to 90 ˚C. By temperature tuning one of the VBGs to longer wavelengths, the laser could be locked on the main peak of one grating with one of the overlapping side-lobes of the other VBG. The concept is illustrated below in Fig. 4.13.

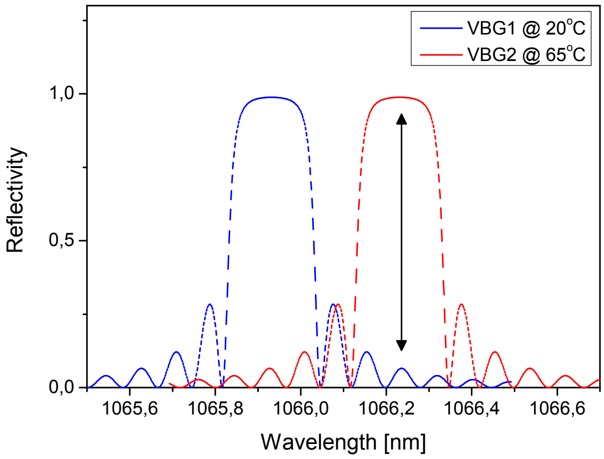

Fig. 4.13. Illustration of spectral overlap between the two VBGs on each side for a temperature difference of 45 degrees. The arrow illustrates a possible oscillation wavelength where VBG1 would be the outcoupler.

The left (blue) curve corresponds to VBG1 while the right (red) curve corresponds to VBG2. In this example, the VBGs have been detuned from each other by 45 ˚C or 0.3 nm and the arrow indicates a possible wavelength the laser can oscillate on. For this wavelength, VBG2 is acting as the highly reflective mirror on one end while VBG1 is acting as output coupler on the other end. The output dynamics of the laser (for a constant pump power) as the VBGs were detuned is shown in Fig. 4.16 below.

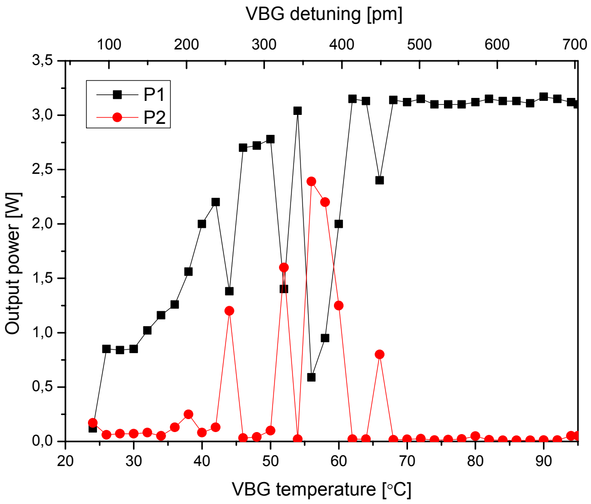

Fig. 4.14. Emission behavior for dual-VBG fiber laser as the two VBGs were detuned.

It can be seen from Fig. 4.14 that the main output is at P1, i.e. in the forward direction (co-propagating with the pump), for a detuning up to 0.2 nm. Between 0.2 nm and 0.5 nm detuning, the main output switches, as it seems, erratically between P1 and P2 only to become stable in the P1 direction again for a detuning larger than 0.5 nm. This behavior is believed to be a result of an asymmetry of the side-lobes, that is side-lobes of the same order do not necessarily have the same amplitude and may also be located at slightly different distances from the main peak. This can be an effect from manufacturing but also induced from absorbed laser radiation [72]. The output power and slope efficiency was measured with the VBGs detuned maximally and compared to an identical cavity employing a normal highly reflective mirror. The result is shown in Fig. 4.15 below.

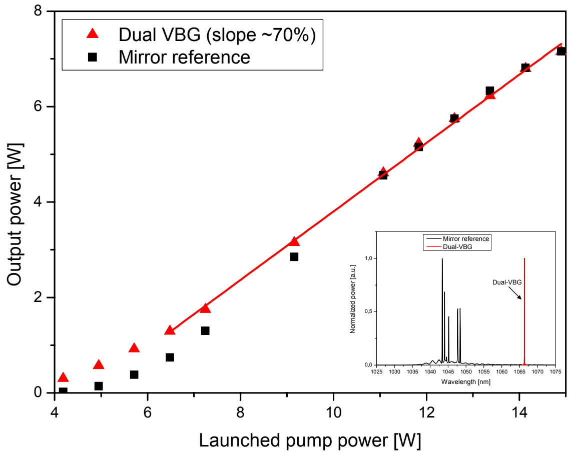

Fig. 4.15. Slope efficiency of dual-VBG fiber laser for a constant detuning of 75 degrees.

For the detuning possible with the temperature controllers used in this experiment, both slope efficiency and output power is very similar to that of a mirror based laser cavity. The spectral output was of course quite different though and is shown in the inset in Fig. 4.15. The linewidth was too narrow to measure using our optical spectrum analyzer so a scanning Fabry-Perot was used instead and it was found to have a linewidth of 2.5 GHz, which is an improvement by a factor of 2 compared to the previous experiment. For better stability, two VBGs should be chosen with an initial separation of ~1 nm and a slight difference in reflectivity of a few percent. This was unfortunately not available at the time of the experiment. Anyway, our simple dual-VBG configuration did not produce a very narrow linewidth but also make it possible to change the feedback of the output coupling dynamically.

4.4 High Power Fiber Lasers

In all the previous experiments described, the output power was limited to less 7 W. One main point of using VBGs together with specialty type fibers such as LMA or PCF fibers is to enable high power narrow linewidth laser emission. Two experiments were therefore designed to better study the operation of VBG based fiber lasers at 1-2 orders of magnitude higher output power. In the first experiment, reported on in Paper IV, a multi mode Er,Yb co-doped fiber was locked with a VBG at normal incidence. The spectral response and the efficiency were compared to a broad band mirror as well as a replica diffraction grating. The fiber we used had a core diameter of 30 μm with a corresponding NA of 0.22, which resulted in a beam quality of $M^2 = 5.5$. As the tuning range of VBGs depend strongly on the beam quality of the incident beam (see Chapter 3), a tuning experiment was also preformed. The VBG had an aperture of 5x7 mm to ensure the whole beam fitted within it. The reflectivity was 96 % at the design wavelength of 1552 nm with a bandwidth of 0.4 nm. The experimental setup for this fiber is shown in Fig. 4.16.

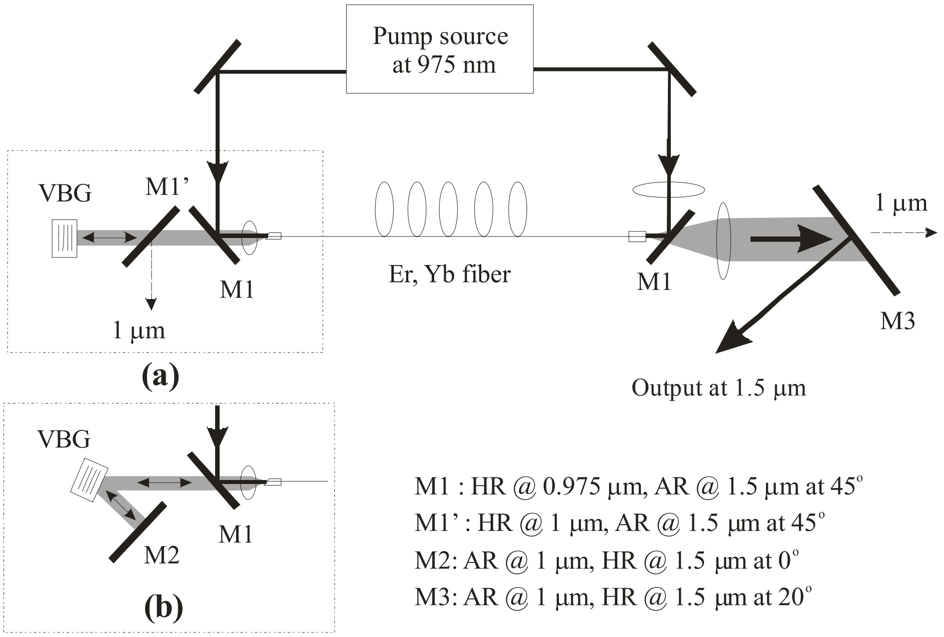

Fig. 4.16. Schematic of experimental setup for Er/Yb-doped fiber laser with high power output.

When the VBG was compared to the free running configuration (where the VBG was replaced by a dielectric mirror), it was found that fiber laser behaved similarly up to a pump power of 150 W. At this point, the free-running fiber laser started to exhibit parasitic lasing at 1.08 μm, resulting in somewhat poorer slope efficiency (see Fig. 4.17). This was a result of higher residual reflections from the dielectric mirror (~5 %) compared to the VBG.

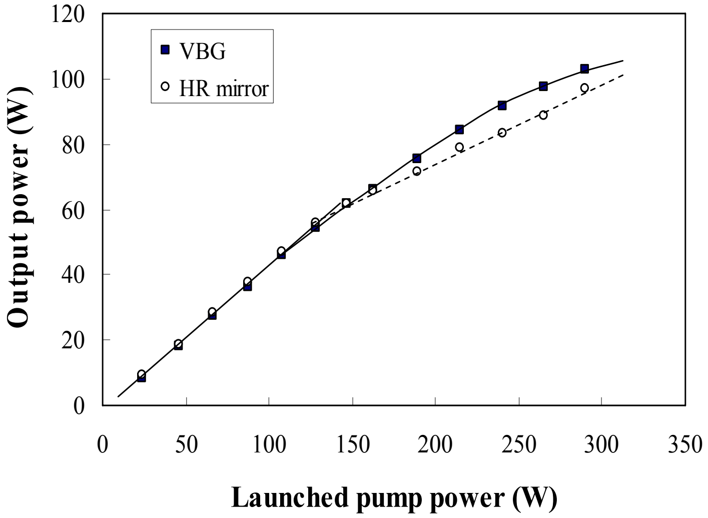

Fig. 4.17. Comparison of slope efficiency for mirror and VBG based systems.

The spectral response of the two cavity configurations (shown in Fig. 4.18) were measured with an optical spectrum analyzer and compared to a cavity configuration were the VBG was replaced with a replica diffraction grating with 600 lines/mm in the Littrow configuration. The linewidths were determined to be 6 nm, 4 nm and 0.4 nm for the free-running, diffraction grating and VBG configuration, respectively. This shows that despite the somewhat poor beam quality, a high efficiency could be achieved with the VBG configuration with a maintained narrow linewidth.

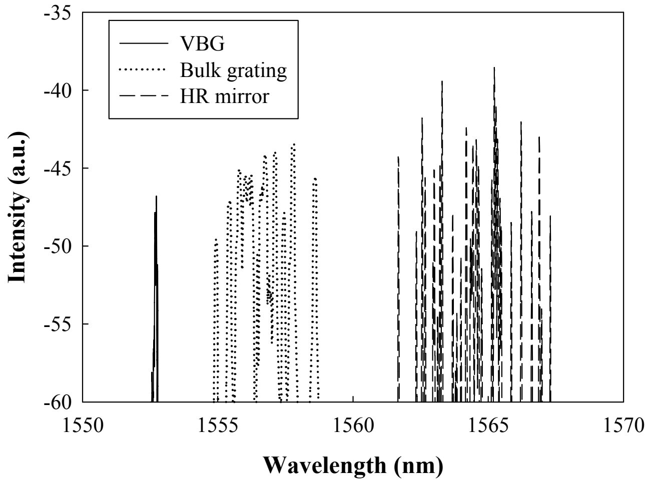

Fig. 4.18. Emission spectrum comparison for VBG, replica diffraction grating and mirror.

By folding the cavity arm with the VBG and using an additional plane broadband mirror (as shown in Fig. 4.16), tunable operation was possible. To avoid parasitic lasing at 1 µm, the pump power was kept at 120 W. It was found that the lasing wavelength could be shifted down as far as 1528 nm where it was limited by the gain of the fiber. The upper tuning limit was 1550 nm where it was limited by the geometry of the cavity. A maximum output power of 38 W was maintained over a range of 15 nm and was just below the output power at normal incidence (41 W) for the same pump power (see Fig. 4.19). The slight difference in output power between normal and oblique incidence can be explained by the double pass in the VBG each round trip which increased the losses in the cavity for the latter case. This double pass configuration also positively affected the linewidth which was reduced to 0.2 nm. It shows that at these power levels, tunable narrow linewidth operation with maintained efficiency is possible using a much more compact setup than with the diffraction grating.

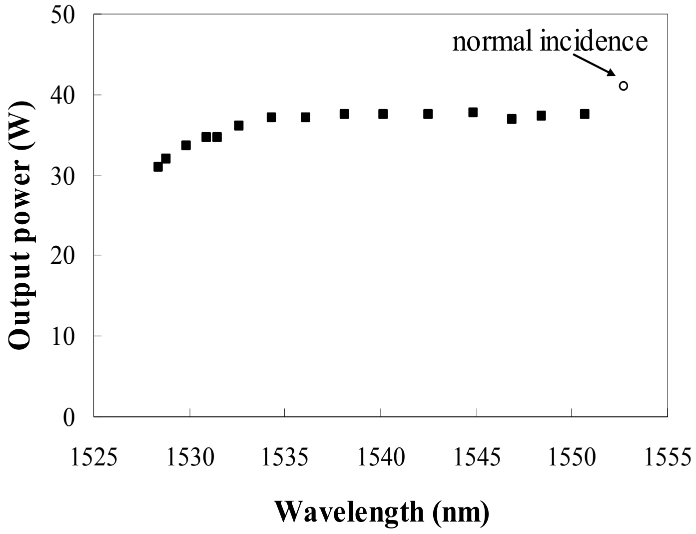

Fig. 4.19.Output power for several wavelengths across the tuning range.

In the second experiment reported on in Paper V, we used on an Yb-doped fiber laser and took advantage of the open design to enable highly polarized emission together with a narrow linewidth. With this configuration, even higher output power was possible and attention was therefore given to possible absorption effects in the VBG (see Chapter 3). The main concern is that absorption in the VBG can cause a distortion in the Bragg structure, which in turn will chirp it and lower the peak reflectivity. The experimental setup is shown below in Fig. 4.20.

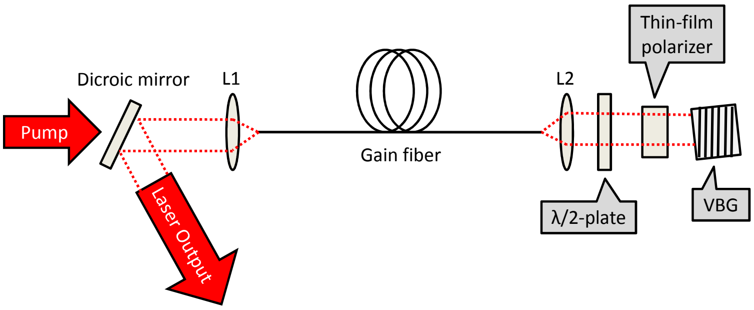

Fig. 4.20. Experimental setup of polarized high power VBG-based fiber laser.

Throughout the experiment, the output power as well as residual transmitted power through the VBG was carefully measured to monitor any signs of heat induced deformation of the grating. As in the previous experiment, this was compared to the lasing properties of a mirror with the same configuration. The fiber used in this experiment had a core diameter of 20 µm with a NA of 0.06 which was low enough to provide close to diffraction limited output. The cladding which had a diameter of 400 µm also contained two stress-rods which induced enough birefringence to make the fiber polarization maintaining. The output power and slope efficiency is shown below in Fig. 4.21.

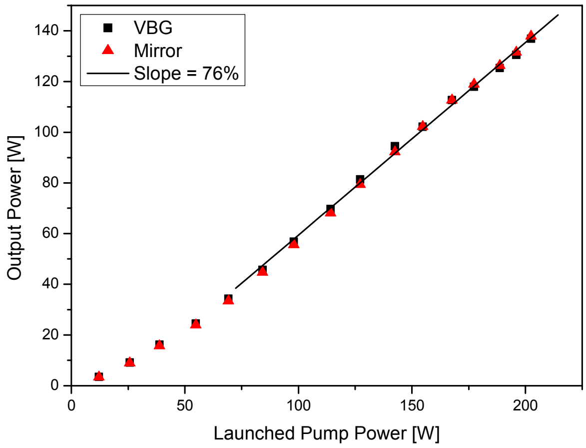

Fig. 4.21. Slope efficiency for VBG and mirror based polarized fiber laser.

It can be seen in Fig. 4.21 that there is no discernible difference in output power between the mirror based setup and the VBG based one. Furthermore, at no time did the residual transmitted signal from the VBG increase more than what would be expected from Rigrod analysis (see Eq. 2.10). The spectral characteristics was also monitored carefully with an optical spectrum analyzer for all power levels and the linewidth of the VBG locked laser was at no point found to go above the design bandwidth of the VBG, which was 0.2 nm. The laser wavelength did however increase from 1065.9 nm at just above the threshold with 4 W of pump to 1066.0 nm for the maximum output power of 138 W at 180 W of pump. This implies that there was no thermal degradation of the grating structure but that a general heating of the VBG took place from direct absorption and/or absorption of scattered light in the VBG holder. This experiment shows that VBGs function well in fiber laser systems at this power level. With a thin-film polarizer and a λ/2-plate in the cavity, a polarization extinction ration of 13 dB was achieved. In all, this makes this type of source very interesting for non-linear conversion processes such as second harmonic generation or sum-frequency generation.

4.5 Cryogenically-Cooled Narrow-Band Temporally-Stable Fiber Lasers

Cryogenic cooling of crystalline laser host materials has been used for a long time to improve material properties such as thermal expansion and thermal conductivity, which strongly affect the beam quality as well as the damage threshold. This is of less importance for fiber lasers since the beam quality is largely defined by the waveguiding structure of the fiber, and the length of the gain medium is quite efficient in dissipating heat, at least for moderate powers on the order of ~100 W. The spectral properties of the amorphous silica host is on the other hand strongly affected by temperature and in Paper VI we show how this can be used to dramatically increase the efficiency and stability of an Yb-doped fiber laser. The increase in efficiency can be understood if we plot the gain cross-section (as defined in Chapter 2) for various inversions at room temperature (dashed lines), and at liquid nitrogen temperatures (solid lines) (see Fig. 4.22 below).

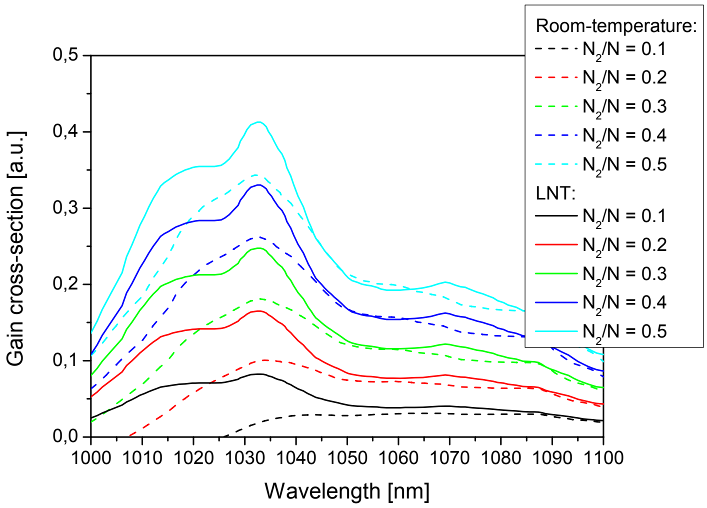

Fig. 4.22. Gain cross-section for an Yb-doped fiber under room-temperature and at liquid nitrogen temperature (LNT) for several inversions [83].

The increased efficiency when cooling comes at the price of a spectrally broad output and a VBG with a design wavelength close to the high gain energy transition at 1032 nm was therefore used to avoid this and lock the laser. Cryogenic cooling of crystalline host materials requires a well controlled environment to avoid problems with condensation and formation of ice on the surfaces of the host. This is not an issue with fiber lasers as the main portion of the gain material can easily be submerged in a coolant without affecting the fiber ends. In our experiment, a simple Styrofoam container was used to hold the liquid nitrogen in which the fiber was submerged. The experimental setup is shown in Fig. 4.23.

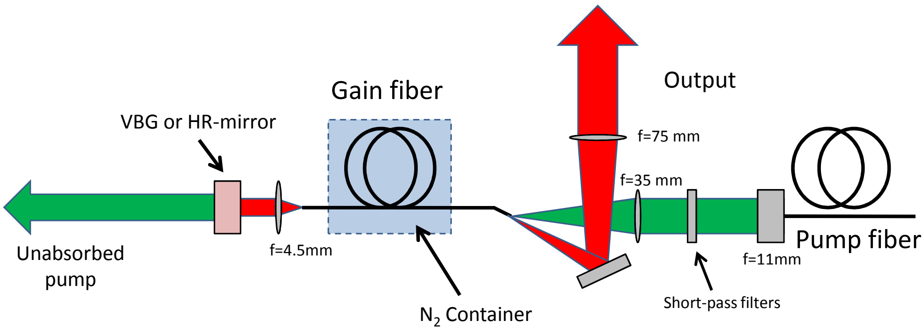

Fig. 4.23. Experimental setup for the cryogenically cooled fiber laser.

At room temperature, it was not possible to use a fiber length longer than ~4 m as self-pulsing otherwise tended to destroy the end-faces of the fiber. In an initial experiment we therefore compared the output power and emission spectrum for this fiber length at room temperature and LNT. It was found that the emission spectrum increased by a factor of 5, from 2 nm to 10 nm, and the output power increased from 7 W to 9 W when the fiber was cooled. The output power and emission spectrum for the two temperature regimes are shown in Fig. 4.24 and Fig. 4.25 respectively.

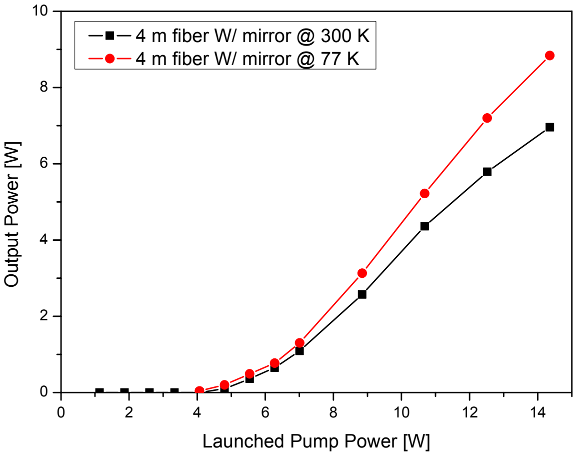

Fig. 4.24. Slope efficiency at room-temperature and LNT for 4 m fiber.

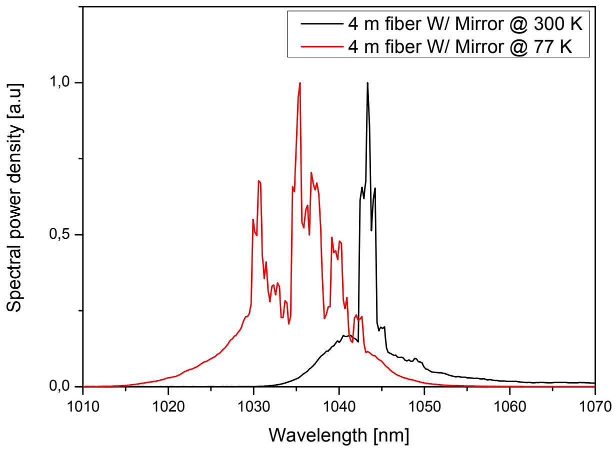

Fig. 4.25. Comparison of spectral emission at room temperature and at LNT for 4 m fiber.

The reduced temperature also proved to efficiently suppress self-pulsing. This is believed to be related to the reduction of the thermal population in the upper stark-levels of the $^{2}F_{7/2}$ manifold implying that that reabsorption at the signal wavelength is almost completely eradicated. This enabled the use of a considerably longer fiber length of 11.5 m, which could almost completely absorb the pump light. For the same launched pump power of 14.5 W, the laser now emitted ~11.6 W at the signal wavelength. The spectral density on the other hand decrease as the linewidth increased to almost 20 nm. The increase in linewidth is believed to be a result of the decreasing homogeneous broadening resulting from the lowered operating temperature. To see if it was still possible to contain all the gain within a narrow linewidth a VBG, with a bandwidth of 0.4 nm and a peak reflectivity of 99 % at 1030 nm was inserted in the cavity, replacing the mirror. The linewidth was now reduced to 0.4 nm, while a marginal decrease in output power was noted (11.4 W compared to 11.6 W). Furthermore, the emission spectrum showed no signs of strong ASE or parasitic lasing outside the grating bandwidth. The output power and emission spectra for the 11.5 m fiber is shown in Fig. 4.26 and Fig. 4.27, respectively, for the two cavity configurations.

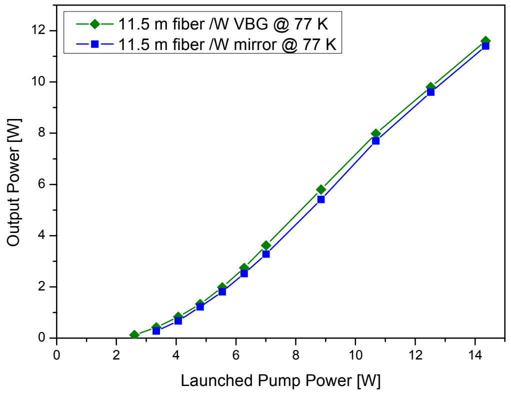

Fig. 4.26. Slope efficiency at LNT for VBG and mirror based fiber laser.

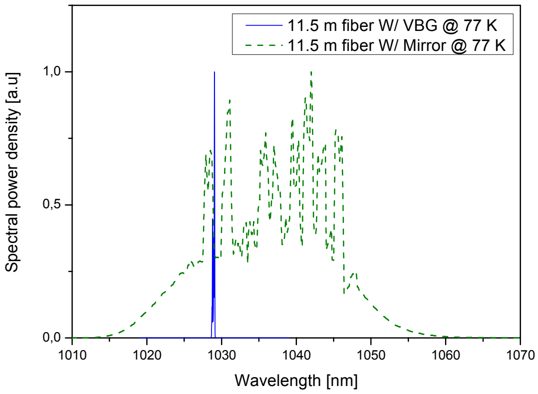

Fig. 4.27. Emission spectrum with VBG and mirror based system.

These results show that cryogenic cooling of Yb-doped fiber lasers is a simple way to stabilize the temporal output as well as substantially increase the efficiency.

4.6 Lasing at 980 nm in a Photodarkening Resistant Silica Fiber

It is commonly known that Yb/Al doped silica fiber lasers suffers from photodarkening. With the proper co-dopant however, the effect can be mitigated. As was discussed in Chapter 2, up until now the most common codopant was phosphorus (P), even though it had detrimental effects on the fiber such as reduced cross-sections, increased brittleness and increased background loss. In Paper VII, it is shown that by cerium (Ce) codoping to a well chosen Yb/Ce-ratio, the photodarkening effect is almost eradicated while other positive properties normally expected from Yb/Al-doped silica fibers are maintained. Three Yb-fibers were drawn with different codopants and/or concentrations: The first fiber denoted Yb/Al, was doped with Yb and Al to a concentration of 0.22 and 2.18 at. %, respectively. The 2nd fiber denoted Yb/Ce/Al I had an Yb/Ce/Al concentration of 0.22 / 0.06 / 2.0 at. % and finally the third fiber denoted Yb/Ce/Al II had an Yb/Ce/Al concentration of 0.55 / 0.55 / 6.86 at. %. In a first experiment the fibers were subjected to 915 nm radiation and the induced loss at 600 nm recorded. The results are shown in Fig. 4.28 below.

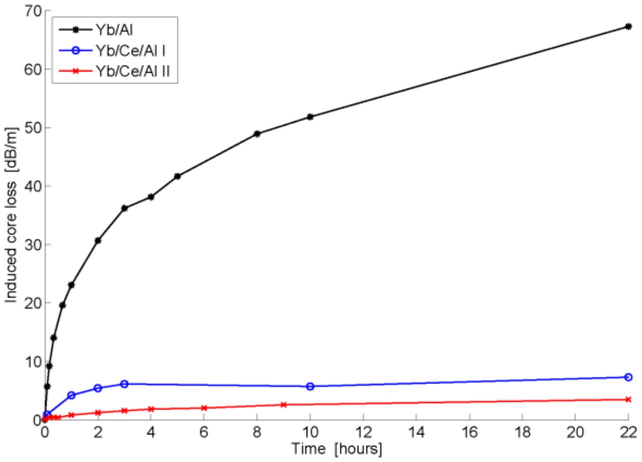

Fig. 4.28. Photodarkening rate for the three different fiber measured as induced loss at 600 nm.

It can be seen that there is a slight difference between fiber Yb/Ce/Al I and Yb/Ce/Al II. If the fibers would not have been codoped with Ce, the results should be the opposite, as photodarkening scales strongly with density of excited ions [62]. To verify that the lasing characteristics were not affected, a simple cavity was constructed and the slope efficiency against absorbed pump was measured. In addition to measuring three unused samples, the Yb/Ce/Al II fiber presented in Fig. 4.28, was also included. The results presented in Fig. 4.29 show only a slight difference between the four fibers.

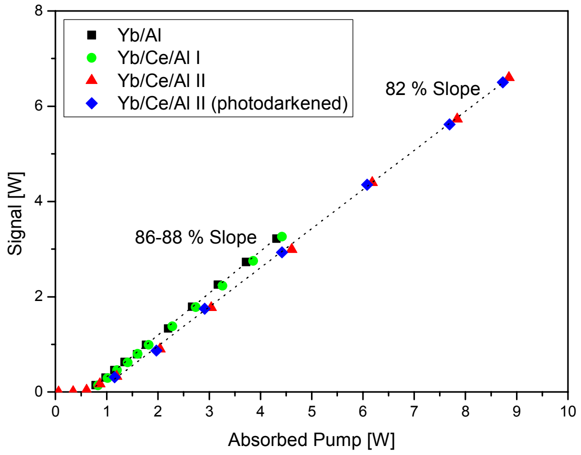

Fig. 4.29. Slope efficiency for the untreated three different fibers together with photodarkened Yb/Ce/Al II fiber from Fig. 4.28.

In all the previous Yb-based experiments described in this chapter, lasing has taken place above 1 µm to one of the upper stark-split levels of the ${}^{2}F_{7/2}$ manifold. Because of this, the requirement on the necessary population inversion to reach transparency, and thus threshold, are not that high, typically only a few percent. In these systems, photodarkening is not generally considered a problem except for industrial laser systems with many thousand hours of expected lifetime. There is however a large interest in high power laser source operating at 980 nm, which coincides well with the 3-level transition between the ground states of the ${}^{2}F_{5/2}$ and ${}^{2}F_{7/2}$ manifolds. From the theory in Chapter 2, it can be understood that this requires a large population inversion, typically close to ~50 %, to achieve transparency, which should greatly affect the photodarkening rate. Little has nonetheless been reported on the long term behavior of Yb-doped fiber lasers emitting at 980 nm. An experiment was therefore designed (Paper VIII) where the Yb/Al, the Yb/Ce/Al I and a commercially available fiber with twice the Yb concentration (0.44 at. %) was compared as gain medium for a fiber laser emitting at 980 nm. The fiber core/cladding diameters were 20/150 µm for the in-house drawn and 30/250 µm for the commercial one. The experimental setup is shown in Fig. 4.30 below.

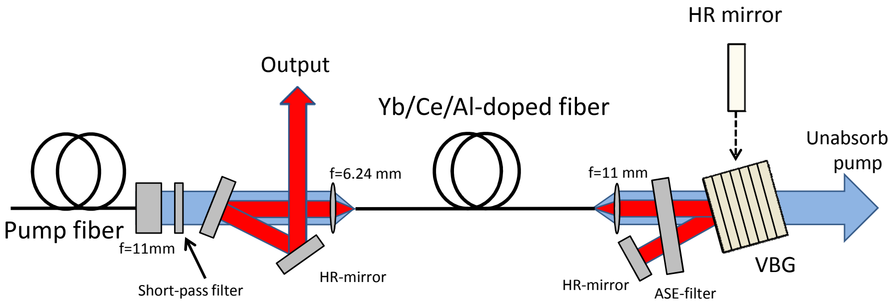

Fig. 4.30. Experimental setup for VBG-based 980 nm fiber laser.

The fiber lengths were chosen to 30 cm for the commercial fiber, 35 cm for the Yb/Al fiber and 45 cm for the Yb/Ce/Al I fiber. The difference in length for the two non-Ce codoped fibers, is motivated by the difference in core and cladding diameter, as the strong parasitic gain above 1 µm depend linearly on the cladding/core area ratio. With the Yb/Ce/Al I fiber, the length was chosen to 45 cm as this was the maximum length possible while still achieving positive gain at 980 nm. In terms of photodarkening, this would in any case increase the photodarkening rate as the longer fiber would require a slightly higher average population inversion along the fiber. The three fibers were in turn placed in a free-running configuration with a highly reflective mirror (AR > 1 µm) as the cavity reflector on one side and the perpendicularly cleaved fiber end on the other. The intra-cavity fiber end closest to the mirror was angle polished to ~10 degrees in order to prevent lasing at 1030 nm. The effect of photodarkening on the output power was measured by monitoring the output power for up to 5 hours. The result is shown in Fig. 4.31 below.

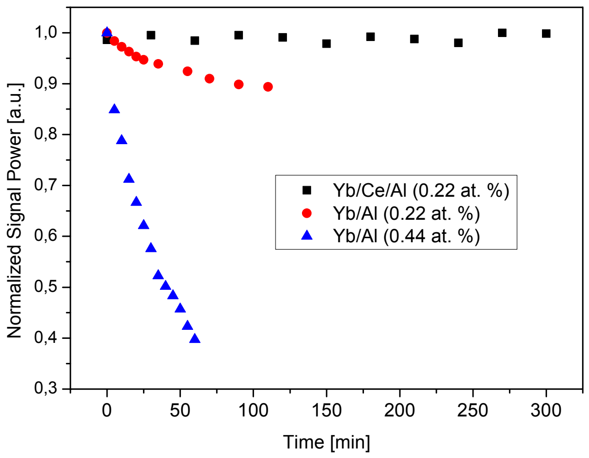

Fig. 4.31. Output power over time for the three different fibers.

As can be seen in the Fig. 4.31, the Yb/Ce/Al I fiber did not shown any noticeable change in output power over the measured time span. The Yb/Al fiber on the other hand showed an instant drop in efficiency and had after ~2 hours dropped to roughly 90 % of its original output power. The commercial fiber, which had twice the concentration of Yb-ions, was expected to degrade faster due to the strong concentration dependence of the photodarkening rate. In fact, it was found that within one hour's time, the output power had dropped to less than 40 % of the original output power.

The emission spectrum of the Yb/Ce/Al I fiber was recorded using an optical spectrum analyzer and it was found to be quite wide with a 6 nm emission linewidth, despite the narrow peak of the emission cross sections at 980 nm compared to the cross-sections above 1 µm. To increase the spectral density, a VBG with a design wavelength of 982 nm was inserted into the cavity as a folding mirror, give a 2-pass spectral filtering each round-trip. The emission spectrum was now below 0.2 nm which was the bandwidth of the VBG. Despite the 2-pass spectral filtering, ASE was still visible in the emission spectrum as can be seen in Fig. 4.32. Nevertheless, Fig. 4.32 also show that the signal to ASE ratio is almost 30 dB, implying that ~99.9 % of the output power is within the 0.2 nm transmission window defined by the VBG.

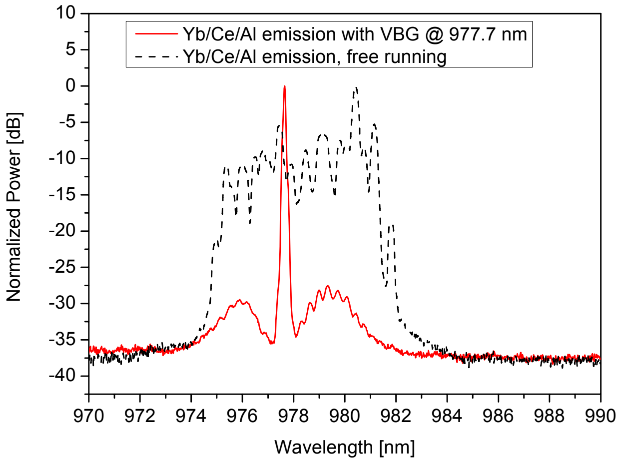

Fig. 4.32. Comparison of emission spectrum at 980 nm for VBG and mirror based setup.

The output power in this experiment was limited to 2 W by the poor pump absorption which was restricted by the fiber length, but also by brightness miss-match between the pump launch fiber and the gain fiber. This resulted in that a considerable amount of pump was launched into the cladding and subsequently into the coating or fiber holder causing catastrophic break-down. With the grating in this configuration, limited wavelength tuning was also possible. The upper limit was set by the normal incidence wavelength of the VBG and the physical restraints on the cavity while the lower was restricted by the gain region of the transition. Fig. 4.33 shows how well the output power could be extracted within the emission window of the VBG. For longer wavelengths, the signal to ASE ratio stays high, but at the other end of the spectrum this ratio drops considerably and is at 975 nm only ~15 dB.

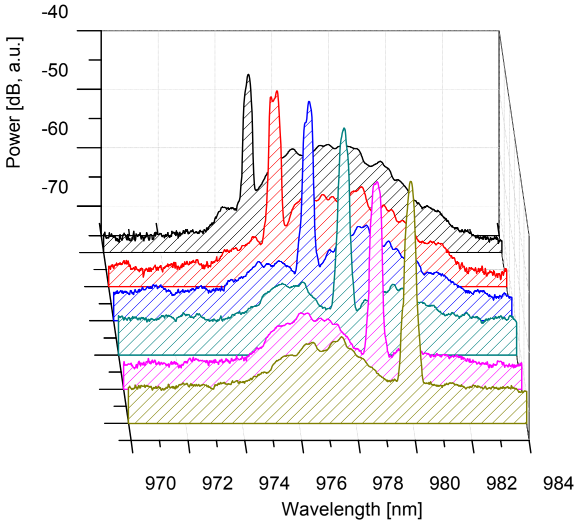

Fig. 4.33. Emission spectrum for several wavelengths within the tuning range.

The detrimental effect from photodarkening on Yb/Al-doped silica fibers limits the usefulness of these fibers in long life-time fiber lasers operating above 1 µm. Furthermore, for the 3-level transition at 980 nm, this effect will quickly degrade the performance of highly doped fibers. With Ce-codoping, degradation free operation over several hours is possible, even at 980 nm. As the photodarkening is believed to only depend on the population inversion density, these results should scale well to higher power and make this fiber composition an excellent candidate as a source for 490 nm generation through SHG [84], in particular so with a VBG for efficient narrowing of the emission linewidth.

5 Conclusions

In this thesis, it is demonstrated how the performance of fiber lasers can be improved with respect to emission spectrum, efficiency, and lifetime. The work addresses the common problems pertinent to high-power fiber lasers and amplifiers. Volume Bragg gratings were extensively studied as spectral filters in fiber lasers and properties such as linewidth narrowing, temperature stability and tunability were characterized. It was shown how a reduction of the fiber temperature substantially increases the efficiency and temporal stability in an Yb-doped fiber laser. Furthermore, it was shown that Ce-codoping of Yb-fibers reduces the photodarkening-rate considerably and increases the life-time of Yb-doped fiber lasers when lasing at wavelengths shorter than 1 μm.

In the first experiment (Paper I), we showed for the first time a VBG-locked fiber laser. A micro-structured Nd-doped silica fiber was used as gain-media in a linear cavity. It was found that it compares favorably to a highly reflective dielectric mirror with a high efficiency (51 % slope) and a narrow emission linewidth (< 0.07 nm). Throughout the experiments, alignment techniques for VBGs were also developed for use with fiber lasers.

This experiment was followed up on using an Yb-doped large-mode area fiber with an order-of-magnitude higher output power (5.5 W). By placing the VBG in a retro-reflector configuration, seamless tunable operation was demonstrated in a compact setup with maintained linewidth over 23 nm. It was also shown that the linewidth (5 GHz) was still contained well within the bandwidth of the VBG. To investigate the short wavelength end of the tuning range, a new pump launch technique, "skew-angle pumping", was developed where the difference in core and cladding NA was used to separate the pump and the signal emission. Furthermore, different coiling techniques were investigated and it was found that the slightly multi-mode core (V-number ≈ 6) could support close to single-mode operation ($M^2<1.3$) when coiled in a folded figure-8 configuration.

For better control of the output coupling, an Yb-doped fiber laser locked with two VBGs was evaluated in Paper III. By using the side-lobes of one VBG as output coupler instead of the end-face of the fiber, a higher spectral selectivity in combination with a tunable reflectivity was achieved. The VBGs, which had almost identical characteristics at room-temperature, was spectrally separated by heating one relative to the other. It was found that for a high enough temperature difference, the output was unidirectional regardless of pump power. An output power of 7 W was achieved with an emission linewidth of 2.5 GHz.

The results from Paper II were scaled another order of magnitude in Paper IV, where an Er/Yb-doped fiber was locked with a VBG at 1552.6 nm. Despite operating in a slightly multi-mode regime ($M^2 \approx 5.5$), tunable operation was realized over 22 nm. With the same identical setup, the VBG was compared to a highly reflective dielectric mirror and a replica diffraction grating. With the VBG, the slope efficiency was increased compared to the mirror (27 % vs. 24 %) for a launched pump power above 150 W. The linewidth was also considerably more narrow (0.4 nm) compared to the grating (4 nm) and the mirror (6 nm), for the same setup.

In Paper V, these experiments were continued with an Yb-doped fiber as gain media. The open design was taken advantage of by including a thin-film polarizer and a half-wave plate. With this arrangement, a high polarization extinction ratio was achieved (13 dB), with a narrow linewidth (< 0.2 nm) at an output power of 138 W with a close to diffraction-limited mode. This type of source could be very useful in non-linear optical applications such as second harmonic generation or sum-frequency generation. Special attention was paid to the temperature stability of the VBG at these power levels. Through careful measurements of the output power and the transmitted power (through the VBG), it was found that no detrimental effects could be seen. Furthermore, by simulating the intensity distribution and heat transfer in a VBG, effects of detrimental heating was identified. These show that a chirping effect might occur at higher powers but that fiber lasers should still be able to handle this quite well compared to low gain solid-state lasers.

In Paper VI, cryogenic cooling was used to increase the efficiency in an Yb-doped fiber laser. With an 11.5 m fiber, 11.4 W of output power was achieved at a pump power of 14.5 W. The high efficiency was a result from an increased absorption cross-section at the pump wavelength, an increased emission cross-section at the signal wavelength as well as a reduced threshold. The cooling of the fiber also increased the temporal stability of the fiber substantially: at room temperature, the fiber used succumbed to catastrophic breakdown of the fiber ends from strong self-pulsing. The increased linewidth at cryogenic temperatures was attributed to a flattening of the gain and a decreased homogeneous broadening. It was mitigated using a VBG with a reflection wavelength close the emission peak of 1032 nm. This experiment showed that cooling of Yb-fiber lasers is a simple way to increase the efficiency as well as the temporal stability.

Photodarkening in Yb-doped fiber lasers is a problem for industrial applications as it reduces the lifespan of the laser. In Paper VII, this problem was addressed by codoping an Yb-doped fiber with Ce. Different Yb/Ce ratios was evaluated and compared to normal Yb-doped fibers. A considerable reduction in photodarkening was attained with the other fiber parameters essentially maintained. This was verified by comparing the power conversion efficiency of an Yb/Al-doped fiber to two Yb/Ce/Al-doped fibers, one of which had been subjected to intense 915 nm radiation. The fibers showed close to identical results.

As the photodarkening-rate depends strongly on the density of excited Yb-ions, emission at 980 nm should be much more vulnerable to this phenomenon as a high inversion is necessary. In Paper VIII, this was evaluated for three different fibers, two of which were drawn in-house and one which was commercially available. One of the in-house drawn fibers was codoped with Ce while the other was not. It was found that the Yb/Ce codoped fiber could sustain degradation-free lasing over the measured time-frame of 5 hours while the two others degraded considerably. The Yb/Ce-doped fiber was also locked with a VBG at 980 nm to evaluate how well the gain could be extracted within the bandwidth of the VBG. A 30 dB signal-to-ASE ratio was achieved with the VBG as a cavity delimiter. This indicates that 99.9 % of the output power was contained within the bandwidth of the VBG (0.4 nm). The experiment shows that the Yb/Ce-codoped fibers are an attractive gain media for 980 nm laser emission and, together with VBG locking, they could be a promising pump source for 490 nm generation through second harmonic generation.

5.1 Outlook

The results from this thesis show that VBGs are a well suited cavity delimiter for fiber lasers. A next natural step of research could be to further scale the output power of fiber lasers and examine whether the spectral characteristics of VBGs are maintained. Despite the growing number of articles detailing how thermal stress can affect VBGs, very few have been verified by experiments. Possible means to study VBGs subjected to intense radiation are thermal cameras, wave front analysis, and holographic measurement techniques.

From an application point-of-view, the next step would be to use the fiber lasers developed in this thesis as pump sources for various non-linear conversion experiments. High power CW second harmonic generation is of great interest as light sources in display systems and projectors. Other interesting non-linear applications could be CW optical parametric oscillators (OPOs) for stand-off measurements techniques such as LIDAR spectroscopy.

References

1. K. C. Kao and G. A. Hockham, "Dielectric-fibre surface waveguides for optical frequencies," Optoelectronics, IEE Proceedings J **133**, 191-198 (1986).
2. E. Hecht, *Optics 4th edition* (Addison-Wesley Publishing Company, 2001).
3. E. Snitzer, "Proposed Fiber Cavities for Optical Masers," J. Appl. Phys. **32**, 36-39 (1961).
4. D. N. Payne, "Active fibres and optical amplifiers," Fiber and integrated optics **11**, 191-219.
5. M. R. J, R. L, J. I. M, and P. David N, "High-gain rare-earth-doped fiber amplifier at 1.54 µm," in *Optical Fiber Communication*, 1987 OSA Technical Digest Series (Optical Society of America, 1987), WI2.
6. S. D. Jackson, F. Bugge, and G. Erbert, "Directly diode-pumped holmium fiber lasers," Opt. Lett. **32**, 2496-2498 (2007).
7. S. Agger, J. Povlsen, and P. Varming, "Single-frequency thulium-doped distributed-feedbackfiber laser," Opt. Lett. **29**, 1503-1505 (2004).
8. H. Zellmer, P. Riedel, and A. Tünnermann, "Visible upconversion lasers in praseodymium-ytterbium-doped fibers," Applied Physics B: Lasers and Optics **69**, 417-421 (1999).
9. B. L. Volodin, S. V. Dolgy, E. D. Melnik, E. Downs, J. Shaw, and V. S. Ban, "Wavelength stabilization and spectrum narrowing of high-power multimode laser diodes and arrays by use of volume Bragg gratings," Opt. Lett. **29**, 1891-1893 (2004).
10. B. Jacobsson, V. Pasiskevicius, and F. Laurell, "Single-longitudinal-mode Nd-laser with a Bragg-grating Fabry-Perot cavity," Opt. Express **14**, 9284-9292 (2006).
11. D. Kouznetsov and J. V. Moloney, "Efficiency of pump absorption in double-clad fiber amplifiers. II. Broken circular symmetry," J. Opt. Soc. Am. B **19**, 1259-1263 (2002).
12. D. Kouznetsov, J. V. Moloney, and E. M. Wright, "Efficiency of pump absorption in double-clad fiber amplifiers. I. Fiber with circular symmetry," J. Opt. Soc. Am. B **18**, 743-749 (2001).
13. D. Kouznetsov and J. V. Moloney, "Efficiency of pump absorption in double-clad fiber amplifiers. III. Calculation of modes," J. Opt. Soc. Am. B **19**, 1304-1309 (2002).
14. M. H. Muendel, "Optimal inner cladding shapes for double-clad fiber lasers," in *Lasers and Electro-Optics, 1996. CLEO '96., Summaries of papers presented at the Conference on*, 1996), 209.

15. J. P. Koplow, D. A. V. Kliner, and L. Goldberg, "Single-mode operation of a coiled multimode fiber amplifier," Opt. Lett. **25**, 442-444 (2000).

16. J. Koponen, M. Laurila, and M. Hotoleanu, "Demonstration of spatial distribution of photodarkening in yb-doped large-mode-area fibre laser," Electron. Lett. **44**, 960-961 (2008).

17. J. C. Knight, "Photonic crystal fibres," Nature **424**, 847-851 (2003).

18. O. Schmidt, J. Rothhardt, T. Eidam, F. Röser, J. Limpert, A. Tünnermann, K. P. Hansen, C. Jakobsen, and J. Broeng, "Single-polarization ultra-large-mode-area Yb-doped photonic crystal fiber," Opt. Express **16**, 3918-3923 (2008).

19. W. Wadsworth, R. Percival, G. Bouwmans, J. Knight, and P. Russell, "High power air-clad photonic crystal fibre laser," Opt. Express **11**, 48-53 (2003).

20. A. Shirakawa, H. Maruyama, K. Ueda, C. B. Olausson, J. K. Lyngsø, and J. Broeng, "High-power Yb-doped photonic bandgap fiberamplifier at 1150-1200 nm," Opt. Express **17**, 447-454 (2009).

21. M. Delgado-Pinar, A. Diez, J. L. Cruz, and M. V. Andres, "High Extinction-Ratio Polarizing Endlessly Single-Mode Photonic Crystal Fiber," IEEE Photon. Technol. Lett. **19**, 562-564 (2007).

22. C. J. Koester and E. Snitzer, "Amplification in a Fiber Laser," Appl. Opt. **3**, 1182-1186 (1964).

23. J. P. Koplow, S. W. Moore, and D. A. V. Kliner, "A new method for side pumping of double-clad fiber sources," IEEE J. Quantum Electron. **39**, 529-540 (2003).

24. R. Herda, A. Liem, B. Schnabel, A. Drauschke, H. J. Fuchs, E. B. Kley, H. Zellmer, and A. Tuennermann, "Efficient side-pumping of fibre lasers using binary gold diffraction gratings," Electron. Lett. **39**, 276-277 (2003).

25. "The Fiber Disk Laser explained," Nat Photon **sample**, 14-15 (2006).

26. M. J. F. Digonnet, *Rare-earth-doped fiber lasers and amplifiers* (CRC Press, 2001).

27. A. E. Siegman, *Lasers*, Lasers, by Anthony E. Siegman. Published by University Science Books, ISBN 0-935702-11-3, 1283pp, 1986. (1986).

28. B. J. Ainslie, S. P. Craig, S. T. Davey, D. J. Barber, J. R. Taylor, and A. S. L. Gomes, "Optical and structural investigation of Nd3+ in silica-based fibres," Journal of Materials Science Letters **6**, 1361-1363 (1987).

29. K. Arai, H. Namikawa, K. Kumata, T. Honda, Y. Ishii, and T. Handa, "Aluminum or phosphorus co-doping effects on the fluorescence and structural properties of neodymium-doped silica glass," J. Appl. Phys. **59**, 3430-3436 (1986).

30. G. Lei, J. E. Anderson, M. I. Buchwald, B. C. Edwards, and R. I. Epstein, "Determination of spectral linewidths by Voigt profiles in Yb3+-doped fluorozirconate glasses," Phys. Rev. B **57**, 7673 (1998).

31. H. W. H. Lee, "Intra-stark relaxation of Nd3+ in silicate glass: Subpicosecond accumulated photon echo experiments," Journal of Luminescence **45**, 99-101.

32. W. L. Barnes, R. I. Laming, E. J. Tarbox, and P. R. Morkel, "Absorption and emission cross section of Er³⁺ doped silica fibers," IEEE J. Quantum Electron. **27**, 1004-1010 (1991).

33. J. N. Sandoe, P. H. Sarkies, and S. Parke, "Variation of Er3+ cross section for stimulated emission with glass composition," Journal of Physics D: Applied Physics **5**, 1788-1799 (1972).

34. D. E. McCumber, "Einstein Relations Connecting Broadband Emission and Absorption Spectra," Physical Review **136**, A954 (1964).

35. W. J. Miniscalco and R. S. Quimby, "General procedure for the analysis of Er3+ cross sections," Opt. Lett. **16**, 258-260 (1991).

36. X. Zou and H. Toratani, "Evaluation of spectroscopic properties of Yb3+ -doped glasses," Phys. Rev. B **52**, 15889 (1995).

37. M. J. F. Digonnet, E. Murphy-Chutorian, and D. G. Falquier, "Fundamental limitations of the McCumber relation applied to Er-doped silica and other amorphous-host lasers," IEEE J. Quantum Electron. **38**, 1629-1637 (2002).

38. R. M. Martin and R. S. Quimby, "Experimental evidence of the validity of the McCumber theory relating emission and absorption for rare-earth glasses," J. Opt. Soc. Am. B **23**, 1770-1775 (2006).

39. Q. Yanbo, D. Ning, P. Mingying, Y. Lüyun, C. Danping, Q. Jianrong, Z. Congshan, and T. Akai, "Spectroscopic Properties of Nd3+-Doped High Silica Glass Prepared by Sintering Porous Glass," Journal of Rare Earths **24**, 765-770 (2006).

40. J. Nilsson, J. D. Minelly, R. Paschotta, A. C. Tropper, and D. C. Hanna, "Ring-doped cladding-pumped single-mode three-level fiber laser," Opt. Lett. **23**, 355-357 (1998).

41. R. Paschotta, J. Nilsson, A. C. Tropper, and D. C. Hanna, "Ytterbium-doped fiber amplifiers," IEEE J. Quantum Electron. **33**, 1049-1056 (1997).

42. R. Kashyap, *Fiber bragg gratings* (Academic Press, 2004).

43. C. H. Liu, A. Galvanauskas, V. Khitrov, B. Samson, U. Manyam, K. Tankala, D. Machewirth, and S. Heinemann, "High-power single-polarization and single-transverse-mode fiber laser with an all-fiber cavity and fiber-grating stabilized spectrum," Opt. Lett. **31**, 17-19 (2006).

44. A. Othonos, "Fiber Bragg gratings," Review of Scientific Instruments **68**, 4309-4341 (1997).

45. Y. Wang, H. Bartelt, S. Brueckner, J. Kobelke, M. Rothhardt, K. Mörl, W. Ecke, and R. Willsch, "Splicing Ge-doped photonic crystal fibers using commercial fusion splicer with default discharge parameters," Opt. Express **16**, 7258-7263 (2008).

46. D. Y. Shen, J. K. Sahu, and W. A. Clarkson, "Highly efficient Er,Yb-doped fiber laser with 188W free-running and > 100W tunable output power," Opt. Express **13**, 4916-4921 (2005).

47. M. Engelbrecht, D. Wandt, and D. Kracht, "Tunable, [mu]s-pulsed ytterbium fiber laser system with a linewidth below 2.7 GHz," Opt. Commun. **279**, 173-176 (2007).

48. C. R. Giles and E. Desurvire, "Modeling erbium-doped fiber amplifiers," Lightwave Technology, Journal of **9**, 271-283 (1991).

49. W. W. Rigrod, "Homogeneously broadened cw lasers with uniform distributed loss," in *Journal Name: IEEE J. Quant. Electron.; (United States); Journal Volume: QE-14:5,* (1978), pp. Medium: X; Size: Pages: 377-381.

50. J. Boullet, Y. Zaouter, R. Desmarchelier, M. Cazaux, F. Salin, J. Saby, R. Bello-Doua, and E. Cormier, "High power ytterbium-doped rod-type three-level photonic crystal fiber laser," Opt. Express **16**, 17891-17902 (2008).

51. F. Roeser, C. Jauregui, J. Limpert, and A. Tünnermann, "94 W 980 nm high brightness Yb-doped fiber laser," Opt. Express **16**, 17310-17318 (2008).

52. V. Pureur, L. Bigot, G. Bouwmans, Y. Quiquempois, M. Douay, and Y. Jaouen, "Ytterbium-doped solid core photonic bandgap fiber for laser operation around 980 nm," Applied Physics Letters **92**, 061113-061113 (2008).

53. A. V. Smith and B. T. Do, "Bulk and surface laser damage of silica by picosecond and nanosecond pulses at 1064 nm," Appl. Opt. **47**, 4812-4832 (2008).

54. F. Brunet, Y. Taillon, P. Galarneau, and S. LaRochelle, "A Simple Model Describing Both Self-Mode Locking and Sustained Self-Pulsing in Ytterbium-Doped Ring Fiber Lasers," J. Lightwave Technol. **23**, 2131 (2005).

55. M. Salhi, A. Hideur, T. Chartier, M. Brunel, G. Martel, C. Ozkul, and F. Sanchez, "Evidence of Brillouin scattering in an ytterbium-doped double-clad fiber laser," Opt. Lett. **27**, 1294-1296 (2002).

56. S. D. Jackson, "Direct evidence for laser reabsorption as initial cause for self-pulsing in three-level fibre lasers," Electron. Lett. **38**, 1640-1642 (2002).

57. A. Hideur, T. Chartier, C. Özkul, and F. Sanchez, "Dynamics and stabilization of a high power side-pumped Yb-doped double-clad fiber laser," Opt. Commun. **186**, 311-317 (2000).

58. W. Guan and J. R. Marciante, "Complete elimination of self-pulsations in dual-clad ytterbium-doped fiber lasers at all pumping levels," Opt. Lett. **34**, 815-817 (2009).

59. F. Shenggui, F. Xinhuan, S. Libin, G. Zhancheng, J. Xiujie, Z. Ying, Y. Shuzhong, and D. Xiaoyi, "Self-pulsing dynamics of high-power Yb-doped fiber lasers," Microwave and Optical Technology Letters **48**, 2282-2285 (2006).

60. M. J. Söderlund, J. J. Montiel i Ponsoda, J. P. Koplow, and S. Honkanen, "Thermal bleaching of photodarkening-induced loss in ytterbium-doped fibers," Opt. Lett. **34**, 2637-2639 (2009).

61. I. Manek-Hönninger, J. Boullet, T. Cardinal, F. Guillen, S. Ermeneux, M. Podgorski, R. Bello Doua, and F. Salin, "Photodarkening and photobleaching of an ytterbium-doped silica double-clad LMA fiber," Opt. Express **15**, 1606-1611 (2007).

62. J. Koponen, M. Söderlund, H. J. Hoffman, D. A. V. Kliner, J. P. Koplow, and M. Hotoleanu, "Photodarkening rate in Yb-doped silica fibers," Appl. Opt. **47**, 1247-1256 (2008).

63. S. Jetschke, S. Unger, A. Schwuchow, M. Leich, and J. Kirchhof, "Efficient Yb laser fibers with low photodarkening by optimization of the core composition," Opt. Express **16**, 15540-15545 (2008).

64. O. M. Efimov, L. B. Glebov, L. N. Glebova, K. C. Richardson, and V. I. Smirnov, "High-efficiency Bragg gratings in photothermorefractive glass," Appl. Opt. **38**, 619-627 (1999).

65. L. B. Glebov, N. V. Nikonorov, E. I. Panysheva, G. T. Petrovskii, V. Tunimanova, and V. A. Tsekhomskii, "New ways to use photosensitive glasses for recording volume phase holograms," Optics and Spectroscopy **73**, 237-237 (1992).

66. L. B. Glebov, "Volume Bragg Gratings in PTR Glass--New Optical Elements for Laser Design," in *Advanced Solid-State Photonics*, OSA Technical Digest Series (CD) (Optical Society of America, 2008), MD1.

67. J. Lumeau, L. Glebova, and L. B. Glebov, "Influence of UV-exposure on the crystallization and optical properties of photo-thermo-refractive glass," J. Non-Cryst. Solids (2007).

68. L. B. Glebov, "High-brightness laser design based on volume Bragg gratings," in *Laser Source and System Technology for Defense and Security II*, (SPIE, 2006), 621601-621610.

69. J. W. Zwanziger, U. Werner-Zwanziger, E. D. Zanotto, E. Rotari, L. N. Glebova, L. B. Glebov, and J. F. Schneider, "Residual internal stress in partially crystallized photothermorefractive glass: Evaluation by nuclear magnetic resonance spectroscopy and first principles calculations," J. Appl. Phys. **99**, 083511 (2006).

70. G. B. Venus, A. Sevian, V. I. Smirnov, and L. B. Glebov, "High-brightness narrow-line laser diode source with volume Bragg-grating feedback," Proc. of SPIE **5711**, 167 (2005).

71. H. Shu, "Split step solution in the iteration of the beam propagation method for analyzing Bragg gratings," Appl. Opt. **48**, 4794-4800 (2009).

72. H. Shu and M. Bass, "Modeling the reflection of a laser beam by a deformed highly reflective volume bragg grating," Appl. Opt. **46**, 2930-2938 (2007).

73. H. Shu, S. Mokhov, B. Y. Zeldovich, and M. Bass, "More on analyzing the reflection of a laser beam by a deformed highly reflective volume Bragg grating using iteration of the beam propagation method," Appl. Opt. **48**, 22-27 (2009).

74. H. Kogelnik, "Coupled wave theory for thick hologram gratings," Bell Syst. Tech. J. **48**, 2909-2947 (1969).

75. B. Jacobsson, "Spectral control of lasers and optical parametric oscillators with volume Bragg gratings," (Kungliga Tekniska Högskolan, Stockholm, 2008).

76. F. Havermeyer, W. Liu, C. Moser, D. Psaltis, and G. J. Steckman, "Volume holographic grating-based continuously tunable optical filter," Optical Engineering **43**, 2017 (2004).

77. J. E. Hellstrom, B. Jacobsson, V. Pasiskevicius, and F. Laurell, "Finite Beams in Reflective Volume Bragg Gratings: Theory and Experiments," IEEE J. Quantum Electron. **44**, 81-89 (2008).

78. A. E. Siegman, G. Nemes, and J. Serna, "How to (Maybe) Measure Laser Beam Quality," in *DPSS (Diode Pumped Solid State) Lasers: Applications and Issues*, OSA Trends in Optics and Photonics (Optical Society of America, 1998), MQ1.

79. J. W. Dawson, M. J. Messerly, R. J. Beach, M. Y. Shverdin, E. A. Stappaerts, A. K. Sridharan, P. H. Pax, J. E. Heebner, C. W. Siders, and C. P. J. Barty, "Analysis of the scalability of diffraction-limited fiber lasers and amplifiers to high average power," Opt. Express **16**, 13240-13266 (2008).

80. P. Glas, D. Fischer, M. Moenster, G. Steinmeyer, R. Iliew, C. Etrich, M. Kreitel, L.-E. Nilsson, and R. Köppler, "Large-mode-area Nd-doped single-transversemode dual-wavelength microstructure fiber laser," Opt. Express **13**, 7884-7892 (2005).

81. D. Marcuse, "Curvature loss formula for optical fibers," J. Opt. Soc. Am **66**, 216-220 (1976).

82. Y. Li, S. D. Jackson, and S. Fleming, "High absorption and low splice loss properties of hexagonal double-clad fiber," IEEE Photon. Technol. Lett. **16**, 2502-2504 (2004).

83. T. C. Newell, P. Peterson, A. Gavrielides, and M. P. Sharma, "Temperature effects on the emission properties of Yb-doped optical fibers," Opt. Commun. **273**, 256-259 (2007).

84. D. B. S. Soh, C. Codemard, S. Wang, J. Nilsson, J. K. Sahu, F. Laurell, V. Philippov, Y. Jeong, C. Alegria, and S. Baek, "A 980-nm Yb-doped fiber MOPA source and its frequency doubling," IEEE Photon. Technol. Lett. **16**, 1032-1034 (2004).